ELSEVIER

Journal of South American Earth Sciences 17 (2004) 121–152

Journal of
South American
Earth Sciences

www.elsevier.com/locate/jsames

The backarc mantle lithosphere in Patagonia, South America

Giorgio Rivalenti[a,*], Maurizio Mazzucchelli[a], Angela Laurora[a], Sara I.A. Ciuffi[a], Alberto Zanetti[b], Riccardo Vannucci[b], Carlos A. Cingolani[c]

[a]*Dipartimento di Scienze della Terra, Università di Modena e Reggio Emilia, P.le S. Eufemia, 19, I-41100 Modena, Italy*
[b]*Dipartimento di Scienze della Terra, Università di Pavia and CNR Istituto di Geoscienze e Georisorse, Sezione di Pavia, Via Ferrata, 1, I-27100 Pavia, Italy*
[c]*Centro de Investigaciones Geológicas, Universidad Nacional de La Plata, 644 Calle No. 1, 1900 La Plata, Argentina*

Received 30 March 2004; accepted 25 May 2004

In memory of my son Carlo Rivalenti

Abstract

The backarc Patagonia mantle underwent pervasive regional re-crystallisation that left only remnants of the pre-existing mantle. Anhydrous xenoliths (dominantly lherzolites and harzburgites, few dunites) are predominant. Xenoliths containing hydrous phases (lherzolites and harzburgites, rare wehrlites) abundantly occur only at G. Gregores. Bulk-rock and clinopyroxene trace element patterns range from predominant LREE-depleted, LILE-enriched and variably Nb-depleted, to LREE-enriched patterns, with negative Zr, Hf and Ti spikes when amphibole is present. V-shaped trace element patterns are found only in rare non-recrystallised xenoliths. Trace element abundances in potential melts calculated from clinopyroxene are similar to arc magmas, but in southern Patagonia fade eastwards to E-MORB-like compositions. Trace element characteristics of bulk-rock and pyroxenes are interpreted as the consequence of two processes: (1) melting in the region of thermal inversion of the wedge, triggered by infiltration of hydrous components; (2) reactive porous flow of the melts into the overlaying mantle. The component triggering melting is inferred to be slab-derived in the western occurrences and a garnet-facies, asthenosphere-derived melt in the eastern occurrences as a consequence of wedge thickening. Differences between northern and southern Patagonia are interpreted to be due to variable contribution of slab components to the wedge. Compared to the southern region, slab-derived melts are tentatively attributed to the subduction of older and colder segments of the Nazca plate in the North.

Keywords: Lithosphere; Melting; Percolation; Reaction; Slab

1. Introduction

Samples of the mantle wedge of convergent plate regions are rare; consequently direct evidence of the interaction between slab-derived components and wedge (Kepezhinskas et al., 1995; Parkinson and Pearce, 1998; Zanetti et al., 1999; Bizimis et al., 2000) is also unusual. Abundant occurrences in Patagonia of mantle xenoliths in alkaline volcanic centres located in the backarc region of the Andean subduction zone (Stern et al., 1990), 300–600 km east from the Chile trench provide the possibility to study these processes. Research on Patagonia arc and backarc magmas has released indirect evidence that the mantle wedge, fertilised by slab components, played an important role either as the source of the arc magmas (e.g. adakites, Stern and Kilian, 1996) or as a component of the backarc basalts, believed to be derived from sub-slab sources (plateau and post-plateau basalts, Gorring and Kay, 2001). In the basalts, the latter authors and Stern et al. (1990) recognise an eastward decrease of slab-related geochemical features.

In addition to providing a general overview of the mantle composition in Patagonia, this paper aims at constraining the depletion and metasomatic enrichment processes in the Patagonian mantle. Specifically, we shall check if the variable slab signature of the basalts is recorded also in the mantle wedge, sampled by the xenoliths at variable distances from the trench (Fig. 1). At present, slab-related metasomatism has been proposed only in some of the westernmost occurrences (Kilian et al., 1998) and possibly at Pali Aike (Stern et al., 1989) and Gobernador Gregores (Laurora et al., 2001), whereas carbonatitic metasomatism has been inferred

* Corresponding author. Tel.: +39-59-205-5813; fax: +39-59-205-5887.
E-mail address: riva@unimo.it (G. Rivalenti).

0895-9811/$ - see front matter © 2004 Elsevier Ltd. All rights reserved.
doi:10.1016/j.jsames.2004.05.009

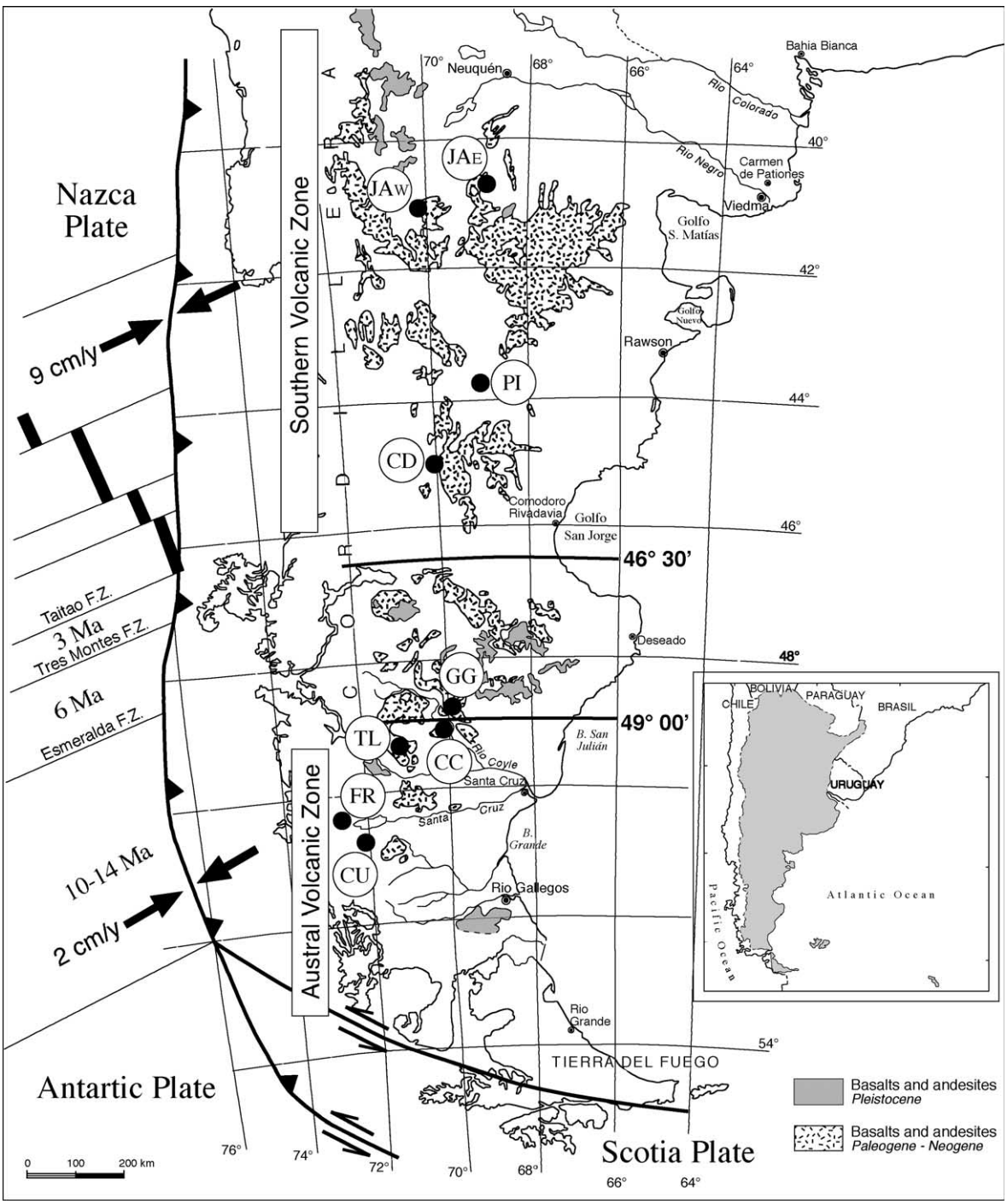

Fig. 1. Sketch map of Patagonia (from the Argentina Geological map and Kay et al., 1993b) showing localisation of the backarc basalts and xenolith occurrences. See text for the acronyms of the localities.

for Gobernador Gregores (Gorring and Kay, 2000) and silicate melt (possibly similar to the host basalt) metasomatism, for Pali Aike (Kempton et al., 1999; Stern et al., 1999).

2. Geological framework and xenolith occurrence

The main geological features of Patagonia (Fig. 1) are summarised by Ramos and Aleman (2000). The Andean volcanic arc is distinguished into a southern volcanic zone (SVZ) and an austral volcanic zone (AVZ, Stern and Kilian, 1996) separated by a volcanic gap between 46.30 and 49°S latitude. The SVZ and AVZ are related to the subduction of the Nazca and the Antarctic plate, respectively. The two plates are separated by the Chile ridge and the present-day triple point between the Nazca, South America and Antarctic plates occurs at 46.30° (Cande and Leslie, 1986; Forsythe et al., 1986). The volcanic gap corresponds with

the northward migration of the triple point, which 14 Ma ago was at approximately 50°S. According to Ramos and Kay (1992); Gorring et al. (1997), the subduction of the Chile ridge induced a slab window in the subducted plate and coincides with the interruption of the volcanic arc. It is possible that another ridge (the Aluk-Farallon) collided during the Eocene at the latitude of the Chubut-Rio Negro provinces (Ramos and Kay, 1992; Kilian et al., 1997; Ramos and Aleman, 2000).

Neogene plateau basalts of tholeiitic to alkaline composition border discontinuously the Andean Cordillera to the east from Rio Negro to the Strait of Magellan (Fig. 1). These basalts are cut by alkaline, OIB-like, post-plateau volcanic centres often bearing xenoliths. According to Stern et al. (1990); Gorring and Kay (2001), both the plateau and post-plateau lava compositions record an eastward decreasing slab component.

The origin of the late Miocene to Pliocene basalts in southern Patagonia was attributed to asthenospheric sources possibly enriched by a weak plume and related to the opening of the slab window (Ramos and Kay, 1992; Gorring et al., 1997; D'Orazio et al., 2000, 2001) and that of the Pleistocene to recent lavas to the thermal and mechanical perturbation induced by the subducted slab in deep lithospheric or asthenospheric levels of the mantle wedge (Stern et al., 1990).

The xenolith-bearing alkaline volcanic centres in northern Patagonia cut the Oligocene-Miocene Somuncura plateau basalts, that extend from 40.5 to 43°S and constitute the largest volcanic pile in extrandean Patagonia. Kay et al. (1993a) suggest they are related to a transient hot spot that affected a mantle whose composition was modified by previous (Eocene) subduction events. De Ignacio et al. (2001) propose their genetic link with asthenospheric corner flow leading to a transient thermal anomaly above the subduction plane.

We examine in this study nine xenolith localities from the Rio Negro to the Santa Cruz provinces. In order to facilitate description, we divide these occurrences in the regions N and S of the present-day triple point at latitude 46.30°S, although this distinction has no geodynamic meaning being unknown, the age of the processes affecting the mantle. The xenolith occurrences (Fig. 1), their co-ordinates, and the acronyms used in the text are as follows. Northern region: Cerro Chenques (CD, 44.52°S, 70.03°W), Cerro del Mojon (JAW, 41.06°S, 70.13°W), Paso de los Indios (PI, 43.48°S, 68.55°W), Estancia Alvarez (JAE, 40.46°S, 68.46°W); Southern region: El Fraile (FR, 50.32°S, 72.41°W), Las Cumbres (CU, 50.42°S, 72.20°W), Tres Lagos (TL, 49.13°S, 71.18°W), Cerro Cuadrado (CC, 48.07°S, 70.08°W), Gobernador Gregores (GG, 48.47°S, 69.56°W).

3. Analytical methods

Bulk-rock analyses were made only on the cores of samples having average diameter >10 cm. These samples were cut into 1 cm thick slabs. Slabs were crushed to 2 mm size in a hardened steel mortar and 100 g of the sand thus obtained was ground in an agate mortar.

Major elements and Sc, V, Cr, and Ni in bulk-rock were analysed on pressed pellets by X-ray fluorescence spectrometry (XRF) at the 'Dipartimento di Scienze della Terra dell'Università degli Studi di Modena e Reggio Emilia', Italy, using a Philips PW1480 XRF. The methods employed were those of Franzini et al. (1975); Leoni and Saitta (1976). Analyses are considered accurate to within 2–5% for major elements, and within 10% for trace elements. FeO was determined as total iron oxide.

Sr, Y, Zr, Nb, Ba, REE, Hf, Ta, Th and U in bulk-rock were analysed by inductively coupled plasma-mass spectrometry at the Department of Earth Sciences of the Memorial University of Newfoundland, St John's, NF, Canada. Full details of the procedure are given in Jenner et al. (1990). Detection limits are reported in Table 1. For quality control, two geological reference standards (gabbro CCRMP MRG-1 and basalt NIST SRM 688) were prepared and analysed with the samples, together with a reagent blank to measure the reagent contribution to the trace element values. Reagent blank concentrations were insignificant for all samples and have not been subtracted from sample concentrations. For most elements, the accuracy of the method (1 r.s.d.), determined from multiple analyses of the reference standards, is 3–7%.

Modes were calculated using the PETMIX programme (available in the web site http://uni-geochem.gwdg.de/docs/binaries.htm) from the chemical composition of the minerals and bulk-rock according to LeMaitre (1979).

Major element, Ti and Cr mineral analyses were carried out at the 'Dipartimento di Scienze della Terra dell'Università degli Studi di Modena e Reggio Emilia', Italy, with an ARL-SEMQ electron microprobe in wavelength dispersive mode, with an accelerating potential of 15 kV, a beam current of 20 nA, and a focused spot size of about 4 μm. Natural minerals were used as standards. Counts were converted to weight percent oxides using the PROBE software by J.J Donovan (Advanced Microbeam 4217 C, Kings Graces road, Vienna, OH 44473, USA). Results are considered accurate within 2–6%.

Trace elements in pyroxenes and amphibole were analysed by laser-ablation microprobe (LAM) ICPMS and secondary ion mass spectrometry (SIMS) at the 'CNR-Istituto di Geoscienze e Georisorse, Section of Pavia'. The (LAM) ICPMS is a double focussing sector field analyser (Finnigan Mat Element) coupled with a Q-switched Nd:YAG laser source (Quantel Brilliant), whose fundamental emission in the near-IR region (1064 nm) is converted to 266 nm by two harmonic generators (Bottazzi et al., 1999). Helium was used as carrier gas, mixed with Ar downstream of the ablation cell. Spot diameter varied in the range 30–100 μm. BCR2-g reference sample was used for calibration, with ^{44}Ca as internal standard for clinopyroxene and amphibole and ^{29}Si for orthopyroxene.

Table 1
Selected bulk-rock major and trace element composition and mode of Patagonian xenoliths

		E. Alvarez	C. Mojon	Paso de los Indios		Cerro de los Chenques			Gobernador Gregores							Tres Lagos			Cerro Fraile		Las Cumbres
		JAE14	JAW37	PI29	PI52	CD21	CD25	CD20	GG54	GG118	GG73	GG92	GG65	GG33	GG86	TL13	TL76	TL57	FR3	FR4	CU12
Group		2	1a	1a	1a	1a	1a	1a	1a	1a	1b	1b	1b	1b	1b	1a	1a	1a	1a	2	2
Lithotype		Ha	Du	Ha	Ha	Lh	Lh	Ha	Lh	Ha	Lh	Lh	Ha	We	We	Lh	Lh	Ha	Lh	Lh	Ha
(Wt%)																					
SiO_2		42.46	41.31	42.26	42.88	43.58	43.54	43.61	45.07	44.70	44.09	42.05	42.46	41.31	41.62	43.75	43.28	43.23	43.32	43.44	41.90
TiO_2		0.02	0.04	0.01	0.01	0.06	0.12	0.05	0.03	0.01	0.02	0.38	0.05	0.12	0.07	0.13	0.12	0.03	0.03	0.03	0.01
Al_2O_3		0.67	1.37	0.67	1.38	1.98	3.17	1.31	1.48	0.54	1.11	2.66	1.24	1.34	1.15	2.99	2.76	0.58	1.50	1.71	0.38
FeO_{tot}		8.08	8.65	8.32	7.96	7.75	8.01	7.89	7.81	7.08	7.83	8.69	7.60	7.96	8.68	7.62	7.86	8.01	8.06	7.88	8.76
MnO		0.13	0.13	0.13	0.12	0.13	0.13	0.13	0.13	0.13	0.14	0.14	0.13	0.14	0.13	0.13	0.13	0.13	0.14	0.13	0.14
MgO		47.06	46.46	47.17	46.15	43.62	41.22	45.25	43.01	45.91	44.77	40.96	44.32	43.38	43.18	41.81	42.02	47.02	44.31	43.95	47.11
CaO		0.67	1.28	0.61	0.73	1.99	2.89	1.01	1.70	0.89	1.15	3.84	3.30	4.59	4.12	2.62	2.90	0.33	1.78	2.08	0.55
Na_2O		0.00	0.00	0.00	0.00	0.09	0.18	0.02	0.02	0.02	0.11	0.38	0.13	0.33	0.28	0.21	0.18	0.00	0.03	0.00	0.02
K_2O		0.03	0.02	0.01	0.04	0.01	0.00	0.01	0.00	0.00	0.03	0.14	0.03	0.05	0.07	0.02	0.01	0.01	0.01	0.00	0.00
P_2O_5		0.00	0.03	0.00	0.03	0.00	0.00	0.00	0.00	0.00	0.02	0.05	0.04	0.03	0.03	0.00	0.00	0.00	0.00	0.00	0.00
Cr_2O_3		0.55	0.41	0.47	0.36	0.50	0.49	0.41	0.45	0.39	0.44	0.46	0.39	0.46	0.37	0.45	0.47	0.30	0.54	0.50	0.78
NiO		0.32	0.30	0.35	0.33	0.29	0.26	0.31	0.30	0.33	0.29	0.27	0.30	0.30	0.30	0.27	0.27	0.37	0.28	0.29	0.35
(ppm)	Det. Lim.																				
Sc	1	5	4	4	4	10	13	7	11	4	6	10	7	9	7	19	15	3	11	12	3
V	3	37	33	30	34	60	75	42	55	19	32	37	35	51	42	62	84	13	64	67	30
Ba	0.30	4.76	13.43	0.90	1.00	1.86	1.08	4.76	4.92	1.37	8.77	32.69	39.99	9.19	33.70	7.43	7.01	3.43	2.84	2.39	2.36
Sr	0.80	4.72	17.59	6.10	4.15	7.09	13.12	8.08	6.87	5.75	31.49	95.58	55.64	83.05	76.95	22.36	14.24	3.64	5.33	2.23	27.85
Ta	0.001	0.033	0.026	0.015	0.008	0.007	0.005	0.013	0.015	0.002	0.186	0.241	0.075	0.337	0.593	0.037	0.012	0.018	0.019	0.007	0.002
Nb	0.005	0.586	0.547	0.339	0.159	0.117	0.088	0.226	0.405	0.055	6.781	5.217	7.336	5.901	9.378	1.020	0.300	0.334	0.239	0.148	0.060
Hf	0.010	0.061	0.318	0.043	0.174	0.231	0.201	0.194	0.188	0.046	0.217	0.714	0.182	0.390	0.510	0.239	0.211	0.242	0.077	0.183	0.035
Zr	0.05	2.06	7.61	1.40	2.96	5.18	6.35	3.69	2.76	0.86	5.68	25.24	5.13	34.63	35.88	7.46	5.81	3.56	2.03	3.39	1.03
Y	0.015	0.160	0.860	0.226	0.203	1.279	2.976	0.808	0.775	0.114	1.404	2.957	1.517	2.828	2.604	2.671	2.912	0.257	0.773	1.094	0.081
Th	0.004	0.052	0.088	0.081	0.026	0.029	0.010	0.121	0.055	0.012	0.076	0.111	0.113	0.096	0.293	0.089	0.039	0.043	0.044	0.060	0.016
U	0.010	0.172	0.051	0.221	0.082	b.d.l.	0.022	0.036	0.022	0.048	0.031	0.124	0.211	0.110	0.095	0.037	b.d.l.	b.d.l.	0.022	0.022	0.055
La	0.020	0.374	0.484	1.077	0.246	0.145	0.181	0.335	0.091	0.074	1.321	2.649	1.630	1.708	3.427	0.737	0.321	0.160	0.296	0.109	0.138
Ce	0.020	0.641	1.115	1.823	0.304	0.378	0.560	0.496	0.324	0.072	3.107	6.899	3.923	5.495	8.837	1.414	0.640	0.271	0.486	0.200	0.112
Pr	0.010	0.092	0.156	0.189	0.046	0.057	0.146	0.085	0.046	0.029	0.515	1.110	0.654	0.933	1.154	0.191	0.135	0.033	0.083	0.022	0.070
Nd	0.020	0.318	0.718	0.570	0.202	0.319	0.662	0.320	0.230	0.056	2.415	5.253	2.814	4.359	5.212	0.891	0.654	0.149	0.289	0.107	0.088
Sm	0.020	0.062	0.173	0.097	0.037	0.106	0.273	0.102	0.062	0.027	0.546	1.212	0.696	1.133	1.226	0.284	0.258	0.038	0.084	0.039	0.043
Eu	0.010	b.d.l.	0.049	0.011	0.010	0.039	0.092	0.031	0.022	b.d.l.	0.168	0.399	0.150	0.354	0.372	0.104	0.095	0.010	0.014	0.010	b.d.l.
Gd	0.020	0.036	0.167	0.048	0.037	0.162	0.375	0.116	0.087	0.011	0.475	1.029	0.481	0.952	1.075	0.379	0.373	0.044	0.081	0.083	b.d.l.
Dy	0.010	0.027	0.157	0.038	0.026	0.221	0.532	0.135	0.121	0.016	0.320	0.729	0.322	0.669	0.698	0.466	0.470	0.041	0.131	0.177	b.d.l.
Er	0.010	0.024	0.094	0.024	0.016	0.146	0.389	0.096	0.087	0.021	0.130	0.295	0.194	0.257	0.224	0.310	0.325	0.023	0.111	0.133	0.026
Yb	0.005	0.023	0.109	0.025	0.025	0.153	0.364	0.096	0.098	0.017	0.097	0.200	0.107	0.154	0.132	0.299	0.320	0.027	0.123	0.166	0.015

Mode (Wt%)																						
Ol	84.7	89.0	86.1	77.9	67.0	55.4	74.0	61.7	74.0	70.1	58.9	77.5	79.6	79.4	61.5	60.4	84.0	75.7	74.7	90.0		
Opx	11.4	4.2	10.7	16.1	22.5	28.0	21.1	30.7	22.3	22.4	27.1	11.5	1.9	1.7	23.2	23.4	14.3	15.3	15.1	6.0		
Cpx	2.4	4.6	2.1	3.5	8.7	14.6	4.2	6.7	3.3	5.6	9.0	4.9	8.2	12.9	12.5	14.4	0.7	7.5	8.7	2.0		
Sp	1.5	2.2	1.0	2.5	1.7	2.0	0.6	0.9	0.4	0.2	0.3	0.2	0.4	tr	1.7	1.3	0.6	1.5	1.5	1.0		
Amph										1.7	2.4	4.2	6.7	3.9								
Phlo											0.3											
Glass										tr	2.0	1.8	3.2	2.1								
Carb										tr	tr	tr										
Ap																						

tr, trace; b.d.l., below detection limit.

Precision and accuracy, both better than 10% for concentrations at the ppm level, were assessed from repeated analyses of SRN NIST 612 reference standard. Detection limits were typically in the range 100–500 ppb for Sc, 10–100 ppb for Sr, Zr, Ba, Gd and Pb, 1–10 ppb for Y, Nb, La, Ce, Nd, Sm, Eu, Dy, Er,Yb, Hf and Ta, and usually <1 ppb for Pr, Th and U.

SIMS analyses were performed with a Cameca IMS 4f on spots of 15–20 μm diameter. Quantification was done by an empirical calibration on a number of well-characterised natural minerals (amphiboles and clinopyroxenes) and using ^{30}Si as internal standard. The primary beam consisted of mass analysed $^{16}O^-$. Analytical conditions were typically 10 nA beam current and 17 keV total impact energy. The ions sputtered from polished, gold coated, samples were transferred to the mass spectrometer by the 25 μm optics and energy filtered by applying -100 V offset voltage, with an energy bandwidth by ± 25 eV. Further details on the analytical and quantification procedures are reported by Bottazzi et al. (1994). Estimated accuracy is $\sim 10\%$ for element concentration at the ppm level.

4. Petrography

The largest xenoliths were found as loose boulders in pyroclastic deposits at Tres Lagos, G. Gregores (up to 60 cm in diameter) and C. Chenques (where they were ejected as bombs coated by a lava shell). In all other localities, xenoliths are hosted in basalts and only samples with sharp contacts against the lava were collected. All the xenoliths here examined are in spinel-peridotite facies.

The xenoliths are distinguished into two groups having medium to coarse-grained granular or porphyroblastic (group 1, Figs. 2B and C) and protogranular or porphyroclastic (group 2, Fig. 2D) texture, respectively. Group 1 is further divided in xenoliths that either do not contain (group 1A, Figs. 2B and C) or do contain (group 1B, Fig. 2E) amphibole ± phlogopite ± apatite. Group 1A xenoliths are predominant in all the localities, except Estancia Alvarez. Group 1B is abundantly represented only at G. Gregores. Representative modal compositions are reported in Table 1 (see the web site: http://www.terra.unimo.it/download/Petrografia/rivalenti/ for a complete data set). Both groups 1A and B mostly consist of lherzolites, harzburgites and minor dunites (Fig. 2A), but three group 1B xenoliths of G. Gregores are wehrlites (Fig. 2A). In both the 1A and B groups, all mineral phases are typically unstrained, except olivine that may show kinks. Grain boundaries are curvilinear, rectilinear in some cases (at C. Chenques and in group 1B xenoliths of G. Gregores) and grains are interconnected by 120° triple junctions (Figs. 2B, C and E). Cloudy clinopyroxenes, where clouding is caused by submicroscopic exolution lamellae and abundant fluid inclusions (Fig. 2), are common in the group 1A xenoliths at Fraile and Cumbres and occur also at C.

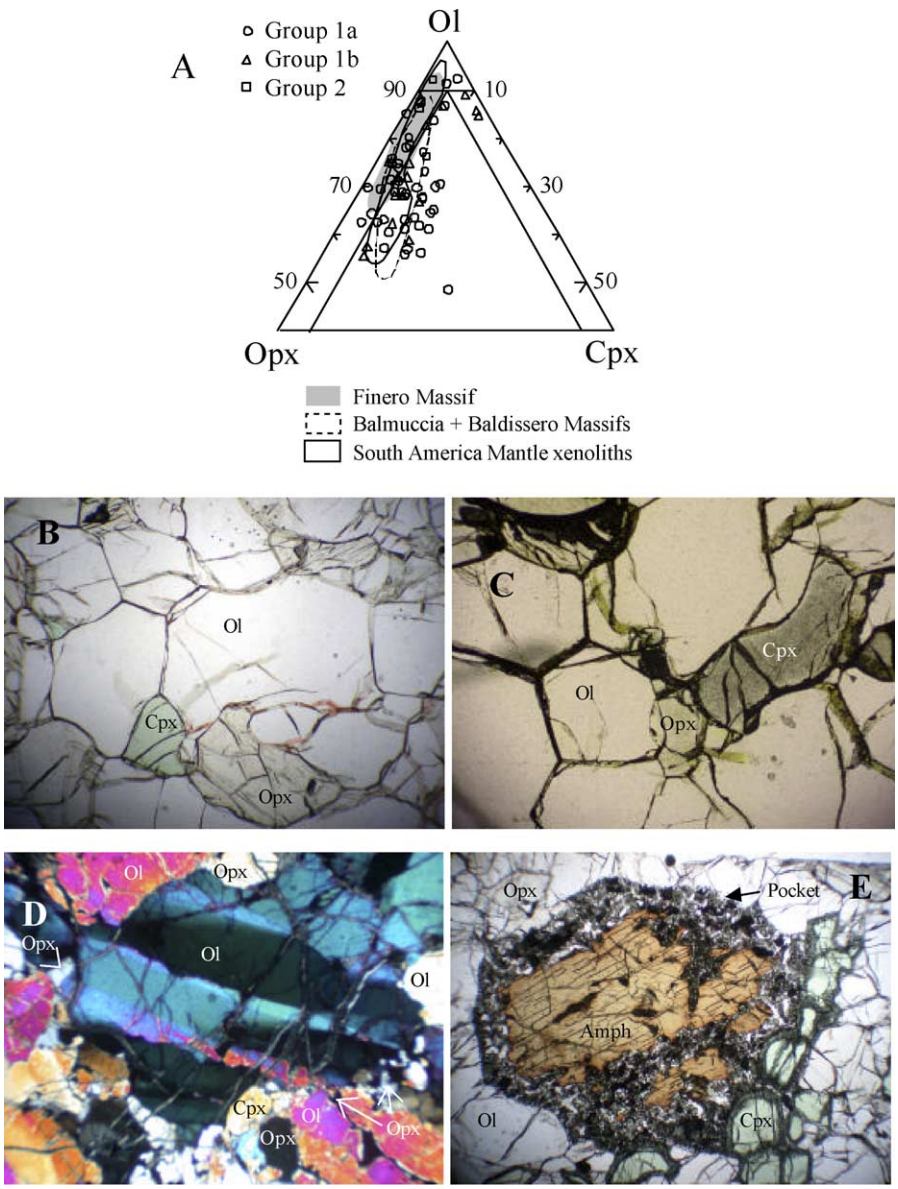

Fig. 2. (A) Modal composition (wt%, see text for the calculation method) of the Patagonia mantle xenoliths compared with peridotite massifs (Rivalenti and Mazzucchelli, 2000), and other South America xenolith occurrences (Rivalenti et al., 2000; Comin-Chiaramonti et al., 2001). Mineral name abbreviations in this and the following figures are as defined by Kretz (1983); (B) Granular texture with 120° junctions (sample CD15, base of the photograph 6 mm); (C) Cloudy clinopyroxene in a granular xenolith (sample FR3, base of the photograph 3.5 mm); (D) Porphyroclastic texture (sample JA14, base of the photograph 6 mm); (E) Partially molten amphibole in a porphyroblastic-textured xenolith (sample GG51, base of the photograph 7 mm); the fine-grained material around and crossing amphibole (pocket) is constituted by glass, carbonate, olivine, clinopyroxene and spinel (Laurora et al., 2001).

Cuadrado and G.Gregores. Exsolved pyroxenes, where exsolution lamellae are clinopyroxene and spinel in orthopyroxene and viceversa, occur only in some group 1A xenoliths and at TL, only clinopyroxene is exsolved. In most cases, orthopyroxene and clinopyroxene are in textural equilibrium. Only in the 1B G. Gregores wehrlites there is clear evidence of clinopyroxene replacing orthopyroxene. Some group 1A lherzolites (CD25, CD61 and GG54) and group 1B lherzolites (GG92, GG49 and GG28) have orthopyroxene concentration exceeding 25 wt% (the modal estimate of Johnson et al., 1990, for primitive mantle) and as high as 35 wt%. Anhydrous (Baker and Stolper, 1994) and hydrous (Hirose and Kawamoto, 1995; Gaetani and Grove, 1998) melting modes in spinel-facies would induce orthopyroxene to decrease in the residues. Only the melting mode of Kinzler (1997) for the high pressure region of the spinel-facies could induce an orthopyroxene increase in the residual peridotite. Reactions forming orthopyroxene by olivine and clinopyroxene dissolution are, however, favoured by the occurrence of olivine and clinopyroxene relics inside orthopyroxene neoblasts at G. Gregores. Furthermore, four group 1A harzburgites (Pi52, Pi29, TL57 and Cu12) and one group 2 harzburgite (Ja14) have olivine concentration exceeding

80 wt% and orthopyroxene in the range 6–14 wt%, thus suggesting that reactions forming olivine at the expenses of clinopyroxene and orthopyroxene also occurred.

Spinel occurs as an intergranular, irregularly-shaped, phase often containing silicate (dominantly olivine) inclusions.

In the 1B xenoliths, amphibole is not in reaction relationship with clinopyroxene, but it is a matrix phase as are the other silicates. At G. Gregores, it is sometimes accompanied by phlogopite and apatite (Table 1). Besides in the samples reported in Table 1 and web site, apatite occurs in the xenoliths Pi16, GG26, GG74 and GG104.

Group 2 xenoliths are represented by six samples only (Ja14, Ja21, Pi41, FR4, CFX and CU12) with protogranular texture and by one porphyroclastic xenolith (Pi14, Fig. 2D). Only group 2 xenoliths occur at Estancia Alvarez. The main differences with group 1, other than texture, are that in group 2 all the mineral phases are strained, pyroxenes are highly exsolved and hydrous metasomatic phases do not occur.

Virtually all the xenoliths contain patent and/or submicroscopic intergranular glass veins and pockets. Laurora et al. (2000, 2001) and Ciuffi et al. (2002a,b) demonstrated these glasses originated due to late events connected with the xenolith residence in the basalts, either from isochemical decompression melting of matrix phases such as amphibole (Fig. 2E), phlogopite and clinopyroxene (Laurora et al., 2000, 2001), or from infiltration of the host alkali basalt (Ciuffi et al., 2002a,b). They do not, therefore, concern the present research and their petrological characteristics will be illustrated in a future paper. However, glass veins originating from melt pockets or from the basalt randomly infiltrate the xenoliths and react with the matrix silicate phases. This may induce a disturbing effect on the bulk-rock and phase geochemistry. While the first cannot be avoided, phase composition has been determined only by spot analyses at the core of the crystals, that should not record interference with glass.

5. Geochemistry

5.1. Bulk-rock

Selected bulk-rock analyses are reported in Table 1. The complete set of analyses used in the text is available on the web site: http://www.terra.unimo.it/download/Petrografia/rivalenti/. Group 1B has been analysed only at G. Gregores.

The TiO_2, Al_2O_3, CaO and Na_2O variation trends with respect to MgO are illustrated in Fig. 3 and compared with other xenolith occurrences of South America (NE Brazil and Paraguay; Rivalenti et al., 2000; Comin-Chiaramonti et al., 2001), peridotite massifs from the Alps (Rivalenti and Mazzucchelli, 2000), abyssal peridotites (Niu, 1997)

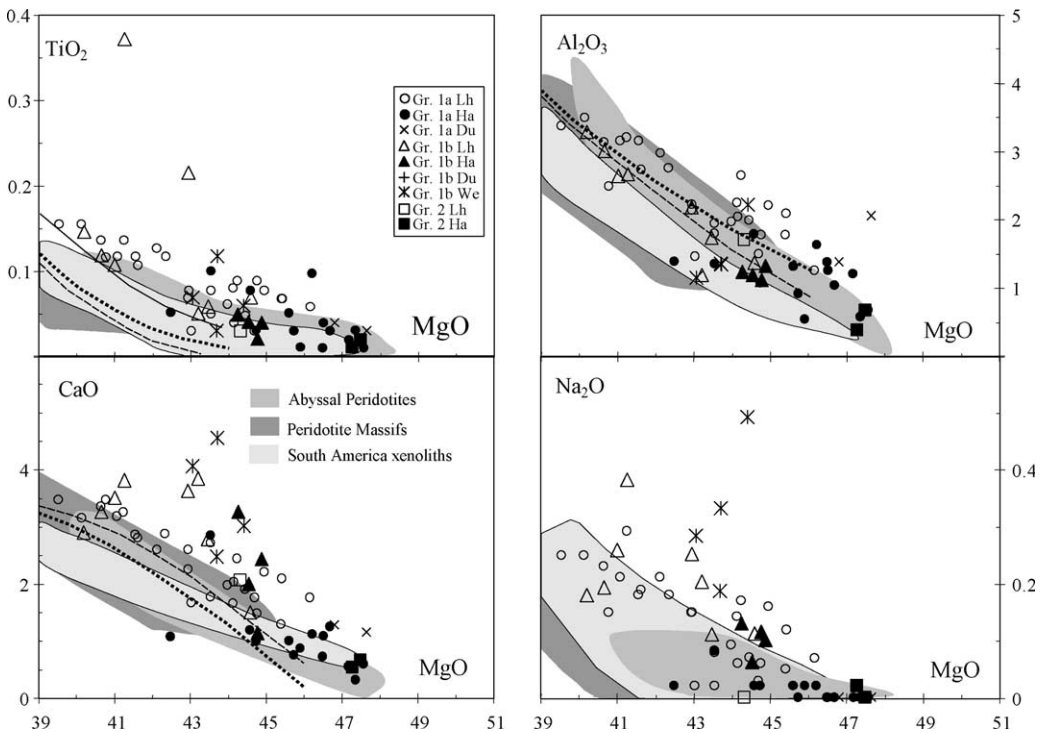

Fig. 3. Major element (wt%) variation trends with respect to MgO (wt%) of the mantle xenoliths of Patagonia compared with the variation in other peridotite occurrences and with the depletion trends modelled by Niu (1997) on two different sources: Ps (dashed lines) and HK93 (dotted lines). The field of the peridotite massifs and South America xenoliths refer to analyses made in the same laboratory and with the same methods employed for the Patagonia xenolith analyses. Abyssal peridotites: Niu (1997); Peridotite Massifs: Rivalenti and Mazzucchelli (2000); South America xenoliths: Rivalenti et al. (2000); Comin-Chiaramonti et al. (2001).

and melting-related depletion trends modelled by Niu (1997). The Patagonia group 1A and 2 xenoliths define arrays paralleling those observed in the other peridotite occurrences and the lherzolites have distinctly higher CaO, TiO_2 and Al_2O_3 concentrations than those of the other South American xenoliths and the Niu (1997) model trends, at the upper concentration limit of the composition of the peridotite massifs.

Group 1B xenoliths have, at a given MgO concentration, lower TiO_2 and Al_2O_3 and higher CaO and Na_2O than those of the group 1A. Two 1B lherzolites and one wehrlite from G. Gregores deviate from the global array towards higher TiO_2 (Fig. 3). This TiO_2 enrichment, paralleled by a MgO decrease, is not caused by infiltration of the host basalt because it is reflected also by higher TiO_2 in the matrix phases clinopyroxene, spinel and amphibole.

Primitive mantle (Hofmann, 1988)—normalised extended trace element patterns are illustrated in Fig. 4. The REE pattern of the group 1A xenoliths varies from slightly LREE-depleted [lherzolites, $(La/Yb)n = 0.3–0.97$)] to slightly LREE-enriched [lherzolites, $(La/Yb)n = 1.6–3.6$; harzburgites, $(La/Yb)n = 1.8–6.6$, 29.3 in Pi 29]. LILE (Ba, Th, U and Sr), especially U, are enriched with respect to La. In the harzburgites, Hf and Zr exhibit a positive anomaly. In the LREE-depleted samples, Nb and Ta are slightly depleted with respect to La, while they are slightly enriched in the LREE-enriched xenoliths of the southern region. Bulk-rock trace element profiles of the 1A xenoliths are less LREE-depleted and are LILE-enriched with respect to their host clinopyroxene (see later), thus documenting the disturbing influence of glass, where these elements are especially concentrated (Laurora et al., 2000, 2001; Ciuffi et al., 2002a,b).

The group 1B xenoliths of G. Gregores have trace element profiles resembling those of peridotites that interacted with alkaline melts (Bodinier et al., 1988; Fabriès et al., 1989; Xu et al., 1998; Grégoire et al., 2000) and characterised by highly fractionated [$(Ce/Yb)n = 2.9–17.7$], upward convex [$(La/Ce)n < 1$)] patterns (Fig. 4). Their Ti, Zr and Hf anomalies vary from absent to negative [e.g. $Hf^*/Hf = 0.9–4.7$; $Ti^*/Ti = 0.9–6.5$, where $Hf^*/Hf = (Nd_n + Sm_n)/(2*Hf_n)$ and $Ti^*/Ti = (Gd_n + Dy_n)/(2*Ti_n)$].

5.2. Clinopyroxene

Selected crystal core analyses are reported in Table 2 (complete data set available at the web site: http://www.terra.unimo.it/download/Petrografia/rivalenti/). In the absence of amphibole (e.g. in the group 1A xenoliths), clinopyroxene is the major host for basaltophile major elements and trace elements and provides better information than bulk-rock analyses because cores analyses should not record the disturbing glass influence. All the clinopyroxenes are Cr-diopsides.

Group 1A. Clinopyroxene composition in lherzolites and harzburgites largely overlaps in terms of Al_2O_3, TiO_2, FeO, Na_2O and Mg# [molar $MgO/(MgO + FeO_{tot})$], although lherzolites extend the variation array to more fertile, and harzburgites to less fertile, compositions (Fig. 5). Only the Cr_2O_3 concentration is higher, at a given Al_2O_3, in clinopyroxene from harzburgites and dunites than from lherzolites (Fig. 5). These parameters correlate with each other and the sample scattering in the diagrams of Fig. 5 is caused mainly by different variation trends for the different localities. Although not specifically illustrated in Fig. 5, the C. Chenques and Tres Lagos pyroxenes, at a given Mg#, have higher TiO_2, Al_2O_3, Na_2O concentrations than C. Cuadrado, C. del Mojon, G. Gregores, Fraile and Cumbres. Note that the G. Gregores 1B pyroxenes whose bulk-rock composition resulted enriched in TiO_2 (Fig. 3), plot outside the group 1B $TiO_2–Al_2O_3$ variation array, at higher TiO_2.

The Patagonia clinopyroxenes have a much wider variation range and on average higher Na_2O and Al_2O_3 than clinopyroxene of abyssal peridotites (Johnson et al., 1990; Johnson and Dick, 1992). They also have higher Mg# values, Cr_2O_3, Na_2O and lower TiO_2 and FeO concentrations than the xenoliths reported by Kepezhinskas et al. (1996) for the Kamchatka island arc mantle.

In most localities, clinopyroxenes of both 1A lherzolites and harzburgites have predominantly LREE-depleted patterns, virtually flat in the MREE-HREE range (Fig. 6), that differ from abyssal clinopyroxenes (Johnson et al., 1990; Johnson and Dick, 1992) for a more marked LREE depletion in the latter. Steady variations to LREE-enriched profiles are also common in both rock types. All the clinopyroxenes exhibit variable, but generally modest, negative anomalies of Ti, Zr and Hf, positive spikes of Th and U, weak positive Sr anomaly and are depleted in Nb, Ta with respect to La. Both LILE and HFSE (Nb, Ta, Zr, Hf and Ti) concentrations increase with increasing REE concentration. In all group 1A clinopyroxenes, Yb, Ti and Y concentrations correlate with modal clinopyroxene (not shown), but the other trace elements do not.

Group 1B. Group 1B clinopyroxenes of G. Gregores and C. del Mojon have lower Mg# values and TiO_2 concentration and higher Al_2O_3, FeO, Na_2O and Cr_2O_3 than group 1A clinopyroxene (Fig. 5). Their REE pattern is convex upward, with $(La/Ce)n < 1$ and $(Ce/Yb)n$ ranging 3.5–5.8 at C. del Mojon and 8.8–21.5 at G. Gregores (Fig. 6), resembling that of clinopyroxenes in cumulates from alkali basalts or peridotites infiltrated by alkaline silicate melts (Bodinier et al., 1988; Fabriès et al., 1989; Xu et al., 1998; Grégoire et al., 2000). Except for a higher Nb/La ratio value, they also resemble the Kamchatka clinopyroxenes (Kepezhinskas et al., 1996). All are Nb, Zr, Hf and Ti depleted with respect to REE and are Th and U enriched with respect to Nb. At G. Gregores, where the 1B group xenoliths are more abundant, the HFSE negative anomaly is largely dependent on the HFSE concentration and increases when the HFSE concentration decreases (Fig. 7). It is poorly dependent on the REE concentration, as large variations of the anomaly correspond to small variation of the REE concentration.

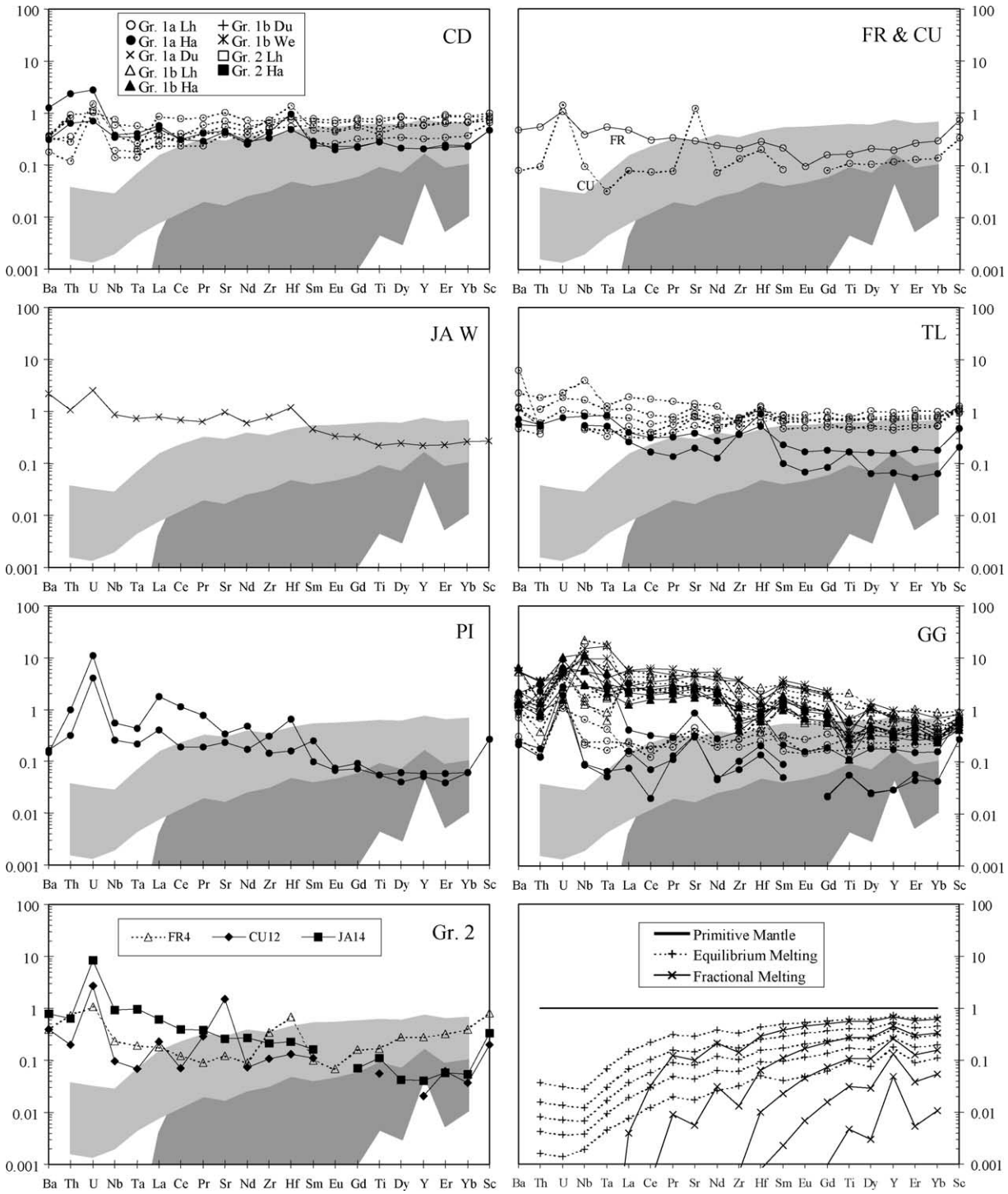

Fig. 4. Primitive mantle (Hofmann, 1988)—normalised incompatible trace element profiles in bulk-rock, compared with models of fractional and equilibrium non-modal melting trends of a primitive mantle (Hofmann, 1988) source. Models are reported at the bottom of the right column and as shaded fields, on the locality diagrams. Lines are 5% melting steps. Parameters in the model: primitive mantle mode: Johnson et al. (1990); melting mode: Gaetani and Grove (1998), (experiment 38–41, Table 9) Melting equations: Shaw (1970). Partition coefficients: from Ionov et al. (2002) for olivine, orthpyroxene and spinel, from Hart and Dunn (1993) for clinopyroxene.

The behaviour of 1B clinopyroxenes is in sharp contrast with that of the 1A group, where (Gd/Ti)*n*, (Nd/Hf)*n* and (Nd/Zr)*n* (the latter not shown in Fig. 7) increase, and (La/Nb)*n* decreases, with increasing both HFSE and REE. The 1A and B trends merge at high HFSE concentration.

Group 2. The six group 2 samples have major element clinopyroxene composition within the range observed in group 1A (Fig. 5). They have spoon-shaped REE patterns, where inflection decreases with increasing REE concentrations (Fig. 6). They also have variable, but negative,

Table 2
Selected clinopyroxene major and trace element composition and olivine and spinel parameters of Patagonian xenoliths

	Estancia Alvarez		Cerro del Mojon				Paso de los Indios			Cerro de los Chenques					Gobernador Gregores					
	JAE21	JAE14	JAW35	JAW50	JAW37	JAW41	PI14	PI18	PI41	CD25	CD34	CD61	CD15	CD28	GG54	GG118	GG73	GG92	GG65	GG33
Group	2	2	1a	1a	1a	1b	1a	1a	2	1a	1a	1a	1a	1a	1a	1a	1b	1b	1b	1b
Lithotype	Lh	Ha	Lh	Ha	Du	Lh	Ha	Ha	Lh	Lh	Lh	Lh	Ha	Du	Lh	Ha	Lh	Lh	Ha	We
(Wt%)																				
SiO_2	54.07	53.99	53.32	53.09	52.03	52.55	53.20	53.83	52.93	52.75	52.66	52.67	53.88	51.10	53.00	54.03	53.25	53.38	53.88	53.57
TiO_2	0.08	0.01	0.26	0.13	0.44	0.44	0.12	0.08	0.06	0.59	0.45	0.46	0.07	0.81	0.15	0.06	0.07	0.23	0.18	0.32
Al_2O_3	1.68	2.03	3.48	3.29	4.21	3.62	2.95	2.91	4.60	6.61	6.19	6.22	3.58	6.71	3.18	2.02	4.76	6.04	5.40	3.85
FeO_{tot}	2.07	2.09	2.50	2.47	2.55	2.78	2.16	1.94	2.31	2.54	2.18	2.28	1.98	2.19	2.37	1.89	2.96	3.66	2.74	2.85
MnO	0.02	0.05	0.04	0.09	0.11	0.15	0.04	0.06	0.06	0.09	0.07	0.09	0.08	0.06	0.08	0.06	0.10	0.10	0.08	0.09
MgO	17.59	18.11	16.38	16.72	16.42	16.79	16.72	16.51	16.73	15.39	14.89	15.05	16.14	15.41	16.84	17.71	15.98	14.40	15.31	15.79
CaO	23.20	22.58	21.29	22.33	22.37	21.93	21.75	22.80	21.22	19.13	20.92	20.37	20.50	20.57	23.06	22.86	18.85	18.18	17.96	19.69
Na_2O	0.52	0.47	1.54	0.80	0.68	0.90	1.11	0.91	1.14	1.95	1.68	1.75	1.59	1.24	0.37	0.46	1.79	2.48	2.56	1.80
Cr_2O_3	0.70	0.57	0.95	0.96	1.06	0.65	1.83	0.94	0.79	0.68	0.71	0.83	1.95	1.66	0.93	0.87	2.21	1.53	1.84	2.02
(ppm)																				
Ba	0.408	0.047	0.416	0.085	0.099	0.033	36.010	0.156	0.196											
Th	0.006	0.003			0.008	0.078	3.390		0.012	0.006		0.021	1.215	0.914	0.016	0.005	0.478	0.265	1.158	0.284
U	0.775	0.003			0.003	0.072	0.736		0.009	0.004		0.007	0.436	0.284	0.005	0.002	0.243	0.068	0.391	0.066
Nb	0.07	0.03	0.21	0.21	0.14	0.11	0.15	0.43	0.22	0.04	0.11	0.03	0.77	0.54	0.05		1.83	0.49	1.90	2.62
Ta		0.057			0.027	0.033	0.054		0.006	0.006		0.012	0.084	0.083			0.113	0.155	0.056	0.553
La	0.10	0.09	9.17	4.88	1.48	3.13	60.46	1.69	0.49	0.79	7.66	0.44	13.41	3.88	0.45	0.06	12.99	12.70	16.74	10.29
Ce	0.25	0.12	20.90	12.74	8.23	12.80	147.61	3.88	0.53	2.98	21.98	1.93	30.14	9.46	1.76	0.13	44.44	47.30	43.80	36.04
Pr	0.02	0.01			1.49	1.85	15.95		0.03	0.61	3.30	0.42	3.18	1.14	0.32	0.03	6.49	7.24	6.66	5.96
Sr	0.9	0.6	313.5	191.1	83.5	144.1	546.0	33.9	13.7	65.2	128.6	40.3	306.5	79.2	22.7	7.5	384.2	333.2	373.4	348.4
Nd	0.07	0.01	13.76	8.55	7.86	8.00	46.69	2.76	0.04	3.93	15.26	2.68	10.44	4.50	1.85	0.37	30.17	30.91	31.06	30.68
Zr	0.2	0.02	44.8	27.1	48.1	20.3	0.7	12.4	0.0	31.0	30.1	20.9	104.6	41.4	5.1	3.2	30.2	89.7	33.3	225.4
Hf	0.03				1.57	0.75	0.03		0.01	1.03	0.78	0.65	2.30	0.44	0.18	0.08	0.10	2.27	1.13	1.74
Sm	0.00	0.00	4.05	1.67	2.40	1.93	7.31	0.74	0.05	1.44	3.08	1.35	2.63	1.16	0.56	0.24	7.67	8.32	8.09	7.76
Eu	0.01	0.00	1.27	0.56	0.86	0.76	2.23	0.28	0.04	0.63	1.13	0.60	0.82	0.44	0.19		2.20	2.32	2.32	2.31
Gd	0.05	0.02	3.31	1.36	2.23	1.87	4.42	0.98	0.18	2.35	3.17	2.04	2.28	1.15	0.60		5.13	5.13	6.36	5.99
Dy	0.14	0.04	2.48	1.02	2.14	1.56	3.42	0.97	0.81	3.42	3.76	2.69	2.06	1.29	0.72	0.51	3.36	3.78	4.33	4.48
Y	1.1	0.5	13.9	5.1	10.6	7.2	24.8	5.8	6.0	18.1	19.8	16.5	9.6	7.2	4.3	2.4	13.1	13.9	16.2	13.2
Er	0.18	0.06	1.27	0.53	1.05	0.75	2.08	0.59	0.74	2.03	2.35	1.70	0.91	0.79	0.46	0.29	1.26	1.63	1.59	1.37
Yb	0.26	0.20	1.32	0.54	1.01	0.57	1.85	0.65	0.85	2.00	2.35	1.65	0.54	0.77	0.49	0.34	0.92	1.11	1.17	0.92
Sc	57.7	49.3	78.9	73.3	42.9	41.1	87.5	82.9	60.1	63.7	69.6	61.7	80.3	59.1	56.2	61.6	63.2	60.8	62.9	58.0
T (°C)	888	1001	926	949	967	991	969	839	1034	1011	961	1029	1034	1086	941	961	1174	1140	1157	1083
Spinel																				
TiO_2	0.10	0.01	0.18	0.11	0.18	0.38		0.06	0.03	0.14	0.05	0.08	0.10	0.12	0.06	0.05	0.06	0.46	0.16	0.78
Mg#	64.5	68.5	66.0	53.8	73.3	67.1		69.9	78.0	79.3	77.5	77.4	68.6	74.0	68.2	62.4	63.0	63.3	69.3	63.8
Cr#	46.0	41.7	42.0	37.3	18.9	35.3		39.6	17.0	9.7	9.7	11.0	48.5	22.5	24.4	47.6	48.2	24.0	37.1	39.7
Olivine																				
Fo	90.5	90.0	91.5	91.0	91.0	91.0		91.5	90.0	88.8	89.7	89.4	91.4	89.9	89.9	91.6	90.5	88.0	91.0	90.1

	Gob. Gregores		Cerro Cuadrado					Tres Lagos							Cerro Fraile			Las Cumbres		
	GG58	GG86	CC3	CC7	CC14	CC8	CC19	TL13	TL50	TL76	TL82	TL2	TL57	TL78	FR3	FR1	FR4	CU21	CU22	CU20
Group	1b	1b	1a	1a	1a	1a	1a	1a	1a	1a	1a	1a	1a	1a	1a	1a	2	1a	1a	1a
Lithotype	We	We	Lh	Lh	Lh	Ha	Ha	Lh	Lh	Lh	Lh	Ha	Ha	Ha	Lh	Ha	Lh	Lh	Ha	Du
(Wt%)																				
SiO_2	53.42	54.16	52.49	52.60	52.84	52.38	52.77	52.40	52.40	52.27	52.73	52.92	53.43	53.18	52.50	52.95	52.07	52.53	52.25	53.64
TiO_2	0.10	0.18	0.57	0.40	0.29	0.45	0.32	0.59	0.67	0.55	0.34	0.16	0.46	0.49	0.16	0.17	0.19	0.21	0.65	0.28
Al_2O_3	6.65	4.96	5.97	4.91	4.26	5.96	4.87	6.78	5.99	6.83	5.77	4.23	4.11	6.06	3.94	3.97	4.87	3.93	4.01	2.38
FeO_{tot}	2.67	3.32	2.12	3.18	2.68	2.21	2.22	2.71	2.20	2.57	2.35	2.27	2.10	2.16	2.48	2.50	2.93	2.71	3.76	2.16
MnO	0.09	0.11	0.07	0.10	0.10	0.08	0.07	0.10	0.07	0.09	0.08	0.08	0.09	0.06	0.12	0.08	0.10	0.05	0.12	0.07
MgO	14.79	15.04	15.17	16.06	18.12	15.26	15.40	15.44	15.82	15.36	15.65	14.91	15.96	15.23	16.60	16.61	15.99	16.54	16.08	16.84
CaO	18.42	17.70	20.59	19.59	20.08	20.82	21.43	19.08	20.01	19.43	20.21	22.47	20.38	19.38	22.35	22.43	21.92	22.51	21.37	22.59
Na_2O	2.49	2.64	1.74	1.44	0.84	1.58	1.39	1.81	1.55	1.73	1.54	1.23	1.63	2.12	0.67	0.58	0.69	0.57	0.73	0.73
Cr_2O_3	1.33	1.86	1.24	1.66	0.70	1.20	1.50	0.77	0.86	0.84	1.04	1.45	1.60	1.05	1.06	0.69	1.21	0.87	1.01	1.30
(ppm)																				
Ba		0.072	0.023	0.104			0.020	0.250	0.469			0.686	1.869		0.044	0.020	0.062	0.037	0.117	0.207
Th	1.277	1.064	0.011	2.017	0.058	0.022	0.036	0.229	0.017	0.073	0.013	0.019	0.286	0.377	0.053		0.361	0.087	0.503	0.133
U	0.387	0.204	0.002	0.441	0.014	0.010	0.013	0.052	0.007	0.055	0.014	0.010	0.092	0.095	0.015		0.135	0.069	0.165	0.136
Nb	0.78	2.81	0.03	1.23	0.14	0.31	0.36	1.38	0.09	0.09	0.11	0.29	0.30		0.06	0.07	0.07	0.04	0.26	0.07
Ta	0.100	0.363	0.005	0.115		0.057	0.051	0.021	0.010	0.017		0.038	0.035	0.011			0.004	0.003	0.027	0.008
La	18.76	18.34	0.82	4.75	0.67	1.05	1.40	2.51	0.72	0.88	0.34	0.59	1.08	6.07	0.11	0.17	0.58	0.36	4.05	0.94
Ce	54.04	48.33	4.08	11.18	2.69	4.24	5.71	5.52	3.43	2.61	1.53	2.42	2.41	10.46	0.35	0.58	0.75	1.43	11.75	3.50
Pr	7.24	6.44	0.84	1.36	0.56	0.84	1.05	0.85	0.75	0.52	0.36	0.53	0.43	1.17	0.07		0.05	0.24	1.63	0.54
Sr	383.4	344.3	75.0	111.4	30.7	79.9	106.3	101.2	65.1	66.0	39.0	56.7	78.6	166.6	13.0	25.0	8.8	9.3	115.8	44.1
Nd	30.75	27.09	4.89	5.27	3.44	4.79	5.44	4.62	4.39	3.44	2.08	3.27	3.52	4.97	0.41	0.67	0.24	1.18	7.81	2.75
Zr	49.4	146.0	34.5	15.1	13.1	31.9	21.3	32.6	25.9	21.1	17.3	11.7	58.4	31.2	1.2	3.9	1.2	2.6	45.0	9.4
Hf	0.67	1.10	1.23	0.38	0.57	0.86	0.63	0.99	1.06	0.69	0.49	0.23	2.51	0.94	0.05		0.07	0.13	1.54	0.24
Sm	7.68	7.16	1.94	1.31	1.39	1.81	1.68	1.96	1.90	1.52	0.99	1.22	1.91	1.36	0.25	0.37	0.25	0.48	2.53	0.92
Eu	2.29	2.18	0.80	0.46	0.57	0.72	0.58	0.77	0.73	0.64	0.47	0.45	0.76	0.51	0.14	0.12	0.12	0.19	0.94	0.40
Gd	5.96	5.97	2.88	1.58	2.11	2.72	1.88	2.62	2.70	2.14	1.61	1.48	2.82	2.11	0.59	1.07	0.63	0.71	2.84	1.23
Dy	3.99	3.69	3.66	1.77	2.71	2.97	2.28	3.18	3.19	2.99	2.65	1.57	2.91	2.44	1.15	1.59	1.17	1.07	2.69	1.58
Y	16.7	16.3	19.6	11.3	15.5	19.2	13.0	19.6	17.3	18.4	17.3	9.4	13.7	14.4	7.7	9.6	7.7	7.6	14.4	10.8
Er	1.69	1.21	2.24	1.10	1.83	1.99	1.37	2.12	1.98	1.95	1.83	0.96	1.38	1.56	0.84	1.38	0.81	0.77	1.38	1.14
Yb	1.51	0.72	1.96	1.05	1.84	1.93	1.30	1.96	1.84	1.88	1.65	0.87	1.13	1.64	0.86	1.17	0.93	0.85	1.26	1.33
Sc	55.4	46.7	65.3	53.1	58.6	66.3	62.0	64.7	77.1	67.3	64.7	68.7	78.5	81.7	66.1	82.0	58.8	59.9	53.2	91.2
T (°C)	1140	1166	993	1143	1193	996	940	1152	1102	1136	1083	761	1041	1080	973	989	1025	973	1078	932
Spinel																				
TiO_2			0.07	0.30	0.12	0.14	0.12	0.19	0.21	0.16	0.11	0.10	0.34	0.12	0.04	0.06	0.06	0.09	0.77	0.42
Mg#			76.8	72.5	77.7	75.6	70.4	77.5	78.5	79.0	77.7	74.6	71.0	77.0	76.3	76.1	74.5	70.6	54.3	61.4
Cr#			16.8	20.5	11.6	19.9	23.2	11.5	16.9	10.1	15.7	30.4	43.3	18.9	19.1	15.2	17.3	22.0	44.2	53.3
Olivine																				
Fo	90.2	89.5	90.8	90.0	90.1	91.3	89.6	90.2	90.9	88.9	90.4	91.2	91.2	90.1	90.1	90.1	89.7	89.8	88.4	91.3

Blank values, below detection limit (see text). Temperature (°C) calculated according the geothermometer of Brey and Köhler (1990) at 1.8 GPa.

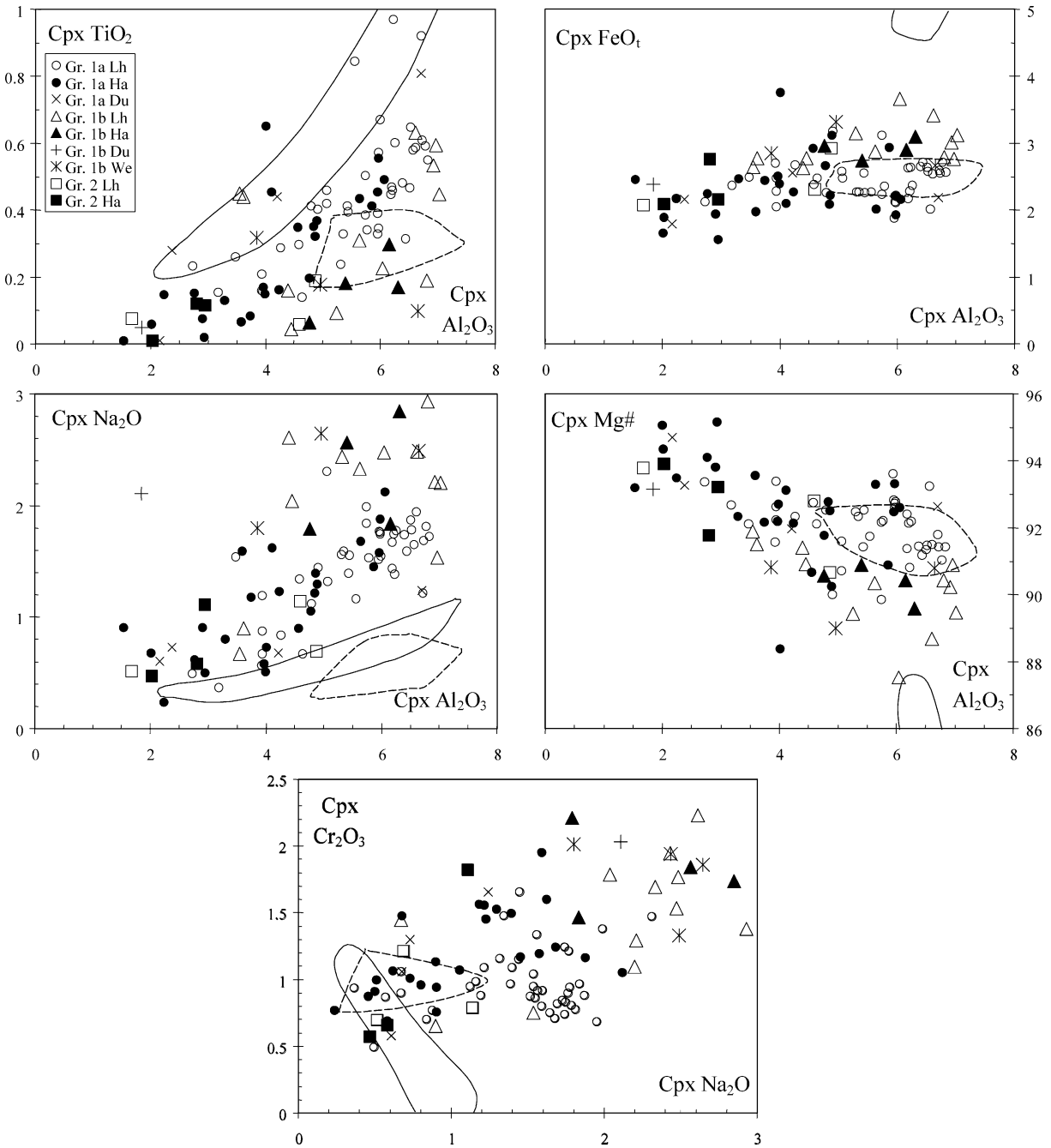

Fig. 5. Major element (wt%) variation trends with respect to Al_2O_3 (wt%) of the xenolith clinopyroxenes, compared with clinopyroxenes in abyssal peridotites (dashed line; Johnson et al., 1990; Johnson and Dick, 1992) and in Kamchatka xenoliths (continuous line; Kepezhinskas et al., 1996).

HFSE anomalies, that are especially relevant in the most REE-enriched sample (Pi14). Like in group 1, Th and U are enriched with respect to Nb. Sr anomaly is distinctly positive in four samples (Fig. 6).

5.3. Orthopyroxene

The major element concentration (selected samples analyses in Table 3, complete data set in the web site: http://www.terra.unimo.it/download/Petrografia/rivalenti/) correlates with that of the coexisting clinopyroxene (examples in Fig. 8A), thus suggesting equilibrium between the two phases. Most orthopyroxenes of 1A harzburgites have higher Cr_2O_3, Na_2O and Mg# and lower FeO_{total} than those of 1A lherzolites.

All the orthopyroxenes are LREE-depleted and with the only exception of Paso de los Indios and of the group 2 Estancia Alvarez orthopyroxenes, exhibit positive Zr, Hf and Ti anomalies (thus accounting for the positive spikes of these elements in harzburgite bulk-rock patterns) and negative Sr anomalies (Fig. 9). Like major element, trace element concentrations of orthopyroxene correlate with

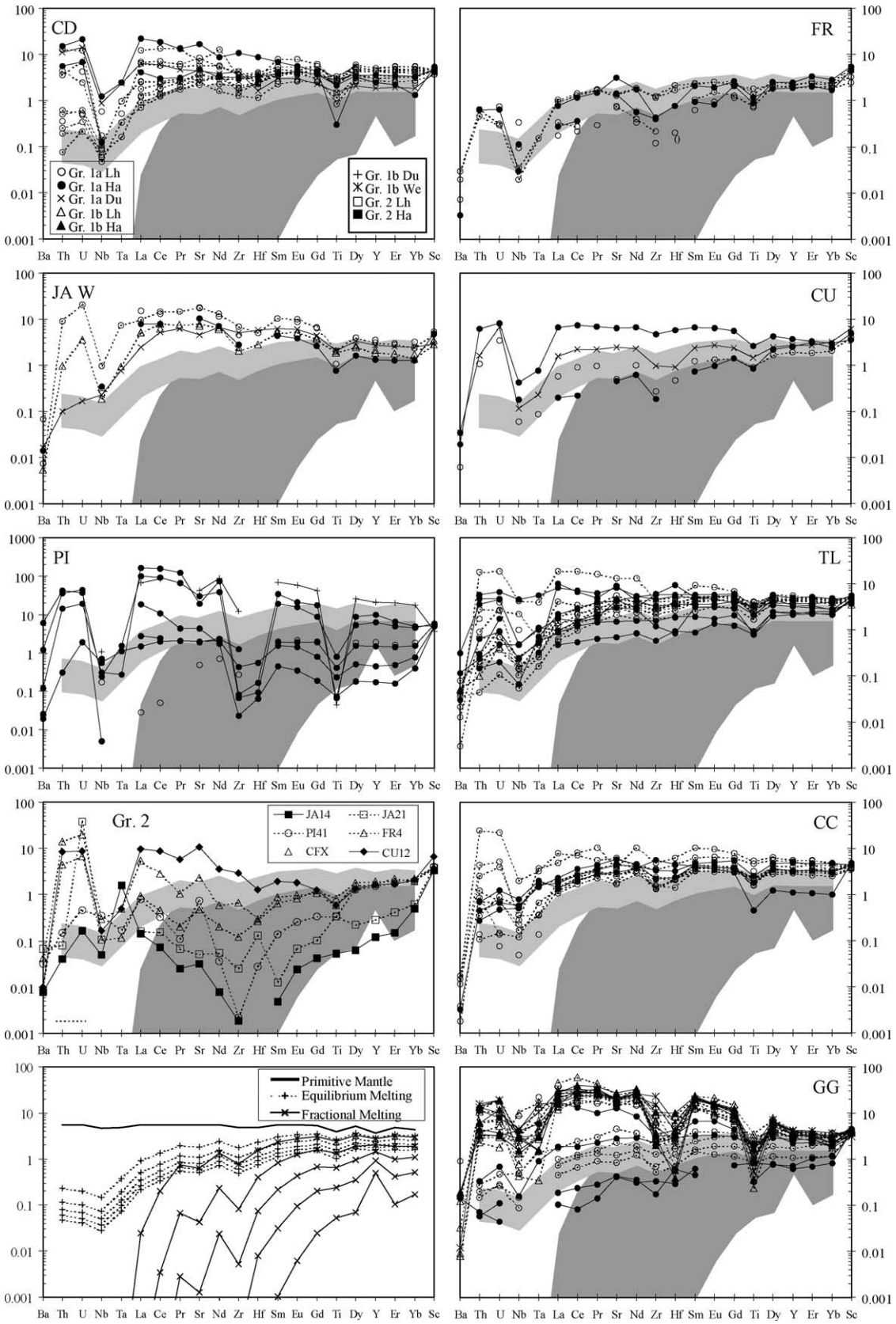

Fig. 6. Primitive mantle (Hofmann, 1988)—normalised incompatible trace element profiles of clinopyroxenes, compared with equilibrium and fractional melting models reported as shaded fields (see Fig. 4 for the parameters used in the models). Lines in the models (bottom of the left column) are 5% melting steps.

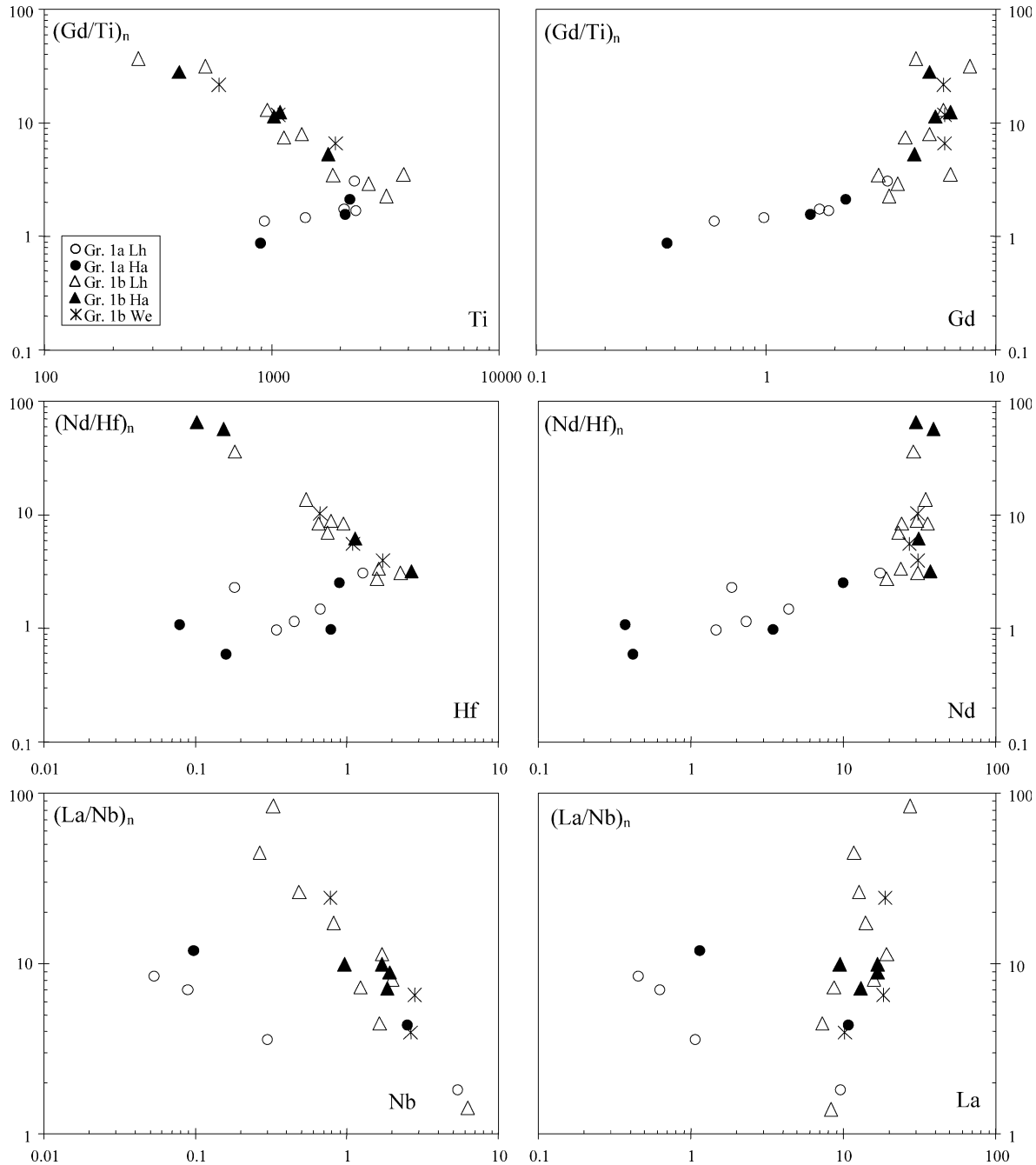

Fig. 7. Correlation of the HFSE anomalies (normalised to the primitive mantle, Hofmann, 1988) with REE and HFSE concentrations (ppm) in the group 1A and B clinopyroxenes at G. Gregores.

those of the coexisting clinopyroxene and by consequence, also the REE fractionation and HFSE and LILE anomalies are correlated (examples in Fig. 8B).

All the incompatible trace elements are preferentially hosted in clinopyroxene. The REE preference for clinopyroxene decreases from Ce to Yb, and is relatively low for Zr, Hf and Ti, thus accounting for the positive spikes of the latter trace elements in extended trace element patterns of orthopyroxene (see also Rampone et al., 1991, for Zr and Ti).

5.4. Olivine and spinel

Important olivine and spinel chemical parameters are reported in Table 2 and in the web site: http://www.terra.unimo.it/download/Petrografia/rivalenti/. Group 1A olivine composition ranges from Fo 87.5–91 in the lherzolites to 89.7–92 in the harzburgites and is relatively constant (Fo 90.2–90.3) in the dunites. In the group 1B lherzolites, olivine range is Fo 88–89.5. Group 2 olivine has Fo value within the group 1 range.

Table 3
Selected orthopyroxene major and trace element composition of Patagonian xenoliths

	Estancia Alvarez		Cerro del Mojon		Paso de los Indios		Cerro de los Chenques				Gobernador Gregores							Cerro Cuadrado		
	JAE21	JAE14	JAW37	JAW41	PI14	PI23	CD25	CD34	CD61	CD15	GG54	GG118	GG73	GG92	GG65	GG33	GG86	CC3	CC7	CC14
Group	2	2	1a	1b	1a	1a	1a	1a	1a	1a	1a	1a	1b	1b	1b	1b	1b	1a	1a	1a
Lithotype	Lh	Ha	Du	Lh	Ha	Ha	Lh	Lh	Lh	Ha	Lh	Ha	Lh	Lh	Ha	We	We	Lh	Lh	Lh
(Wt%)																				
SiO_2	56.23	56.41	55.75			56.42	55.09	55.59	55.46	56.59	55.78	56.76	56.25	54.86	55.77	55.36	56.25	55.65	54.87	55.15
TiO_2	0.02	0.00	0.11			0.01	0.12	0.07	0.09	0.01	0.07	0.03	0.02	0.18	0.06	0.10	0.04	0.10	0.19	0.10
Al_2O_3	1.71	2.07	3.44			1.67	4.29	3.56	3.69	2.14	3.07	1.96	2.42	3.99	3.01	3.84	2.42	3.54	4.08	3.77
FeO_{tot}	5.56	5.61	5.55			5.38	6.36	6.31	6.31	5.10	6.11	5.23	5.91	7.99	6.08	6.09	6.14	5.44	6.30	6.44
MnO	0.17	0.13	0.22			0.22	0.13	0.14	0.16	0.13	0.15	0.14	0.16	0.15	0.11	0.14	0.16	0.12	0.11	0.14
MgO	34.75	34.86	33.85			35.30	32.90	33.51	33.44	34.62	33.72	34.80	33.78	31.45	33.44	32.82	33.52	34.01	32.55	33.59
CaO	0.47	0.43	0.54			0.39	0.63	0.44	0.41	0.63	0.61	0.51	0.63	0.84	0.66	0.90	0.73	0.52	1.02	0.37
Na_2O	0.02	0.03	0.04			0.06	0.11	0.07	0.07	0.09	0.01	0.04	0.13	0.19	0.16	0.18	0.18	0.04	0.06	0.02
Cr_2O_3	0.97	0.34	0.50			0.37	0.31	0.26	0.31	0.62	0.43	0.50	0.65	0.31	0.63	0.53	0.49	0.52	0.80	0.31
(ppm)																				
Ba	0.085		0.097	0.050	1.087	0.063												0.027		
Th			0.091		0.076	0.082					0.005	0.025		0.004	0.006	0.003	0.007	0.001	0.004	0.008
U		0.002		0.002	0.016	0.028				0.007	0.002	0.043	0.003	0.002	0.010		0.001		0.003	0.002
Nb	0.004	0.008	0.050	0.011												0.160	0.103	0.011	0.020	
Ta			0.139	0.001	0.004	0.005			0.039							0.037	0.005	0.003		
La	0.001	0.001		0.002	0.143	0.043				0.016						0.098	0.036	0.008	0.017	
Ce	0.004	0.002	0.018	0.027	0.467	0.055		0.035		0.045			0.072	0.118	0.132	0.378	0.148	0.027	0.079	0.009
Pr			0.002	0.003	0.056	0.003	0.007							0.024		0.078	0.030	0.005	0.015	
Sr			0.089	0.163	2.241	0.229	0.232			0.495			0.642	0.718	0.603	3.365	0.994	0.370	0.347	0.144
Nd			0.032	0.042	0.208	0.009				0.069				0.148	0.173	0.446	0.187	0.033	0.079	0.014
Zr	0.026		3.440	1.084	0.015	0.037	1.699			3.189	0.342		0.775	5.773	0.792	10.135	3.963	1.540	1.431	0.831
Hf	0.004	0.016	0.102	0.046		0.011	0.086							0.119	0.071	0.193	0.027	0.071	0.024	0.051
Sm			0.015	0.022	0.070				0.019				0.032				0.075	0.013	0.026	
Eu			0.009		0.028		0.014									0.057	0.031	0.007	0.010	
Gd			0.055	0.043	0.047												0.113	0.042	0.038	
Dy	0.006	0.003	0.078		0.097		0.137	0.112		0.060			0.108	0.143	0.132	0.216	0.155	0.114	0.063	0.087
Y	0.077	0.029	0.743	0.542	1.016	0.037	1.405	1.042		0.547	0.284		0.666	0.830	0.687	1.005	0.957	0.877	0.603	0.855
Er	0.014	0.006	0.102	0.058	0.100	0.017	0.161	0.096		0.059	0.084			0.086	0.045	0.082	0.095	0.075	0.082	0.128
Yb	0.029	0.031	0.247	0.102	0.208	0.036	0.337	0.332	0.015	0.079	0.164			0.147			0.101	0.220	0.159	0.242
Sc	17.6	19.2	15.1	11.4	12.3	12.4	17.7	14.5	1.4	13.3	19.1	41.6	7.8	8.8	10.5	14.5	8.1	19.0	14.1	20.9

(*continued on next page*)

Table 3 (*continued*)

		Cerro Cuadrado		Tres Lagos				Cerro Fraile		Las Cumbres
	CC8	CC19	TL13	TL2	TL57	TL78	FR3	FR4	CU21	CU22
Group	1a	1a	1a	1a	1a	1a	1a	2	1a	1a
Lithotype	Ha	Ha	Lh	Ha	Ha	Ha	Lh	Lh	Lh	Ha
(Wt%)										
SiO_2	55.26	55.62	54.84	55.79	56.31	55.57	55.50	55.20	55.28	55.43
TiO_2	0.10	0.08	0.14	0.05	0.11	0.11	0.04	0.06	0.05	0.15
Al_2O_3	4.14	3.24	4.65	3.06	2.47	3.61	3.38	3.61	3.64	2.33
FeO_{tot}	5.63	5.84	6.11	5.74	5.20	5.90	6.12	6.47	6.42	8.39
MnO	0.12	0.12	0.13	0.12	0.13	0.13	0.17	0.13	0.04	0.16
MgO	33.43	33.73	32.75	33.72	34.28	33.41	33.58	33.30	33.27	32.36
CaO	0.58	0.60	0.82	0.72	0.70	0.65	0.67	0.69	0.68	0.62
Na_2O	0.07	0.05	0.13	0.08	0.11	0.14	0.05	0.05	0.03	0.02
Cr_2O_3	0.64	0.65	0.37	0.65	0.63	0.44	0.42	0.40	0.52	0.47
(ppm)										
Ba		0.013	0.014						0.031	0.017
Th	0.002		0.003				0.014	0.016	0.002	0.312
U		0.003					0.013	0.007	0.004	0.038
Nb		0.023	0.037				0.008	0.010	0.012	0.034
Ta		0.002						0.001		0.004
La		0.015	0.006				0.006	0.007		0.169
Ce	0.021	0.045	0.018	0.009		0.084	0.013	0.004	0.004	0.475
Pr		0.007	0.002			0.012	0.001	0.001	0.001	0.069
Sr	0.362	0.612	0.253	0.094	0.230	0.492	0.033			4.450
Nd		0.043	0.037	0.008	0.031	0.059		0.004	0.003	0.287
Zr	1.244	0.841	1.860	0.556	2.609	1.447	0.181	0.057	0.172	4.950
Hf	0.040	0.038	0.040	0.012	0.179			0.004	0.009	0.084
Sm	0.015	0.018	0.035	0.005					0.003	0.122
Eu			0.013	0.013		0.027				0.040
Gd		0.033	0.049				0.015	0.016		0.134
Dy	0.087	0.051	0.157	0.053	0.086	0.146	0.064	0.062	0.052	0.175
Y	0.834	0.556	1.280	0.523	0.982	0.982	0.571	0.576	0.514	1.450
Er	0.116	0.073	0.158	0.091	0.092	0.102	0.082	0.081	0.076	0.174
Yb	0.336	0.127	0.207	0.133	0.111	0.292	0.137	0.205	0.202	0.258
Sc	19.2	16.6	17.2	14.8	17.3	19.3	19.6	18.7	20.8	21.6

Blank values, below detection limit (see text).

Spinels (Table 2) show a correlation between Mg# and Cr# [Cr/(Cr + Al + Fe^{3+}) in atoms] values and a variation range similar to that of abyssal peridotites (Fig. 10). Group 1A harzburgitic spinels have the highest Cr# and lowest Mg# values. Spinel composition correlates with that of coexisting olivine and clinopyroxene (Fig. 11). In group 1A lherzolites, Cr# value of spinel increases as the Fo concentration in olivine increases and the HREE (and Y) and Al_2O_3, TiO_2 and Na_2O concentrations of clinopyroxene decrease (Figs. 5 and 11). The spinels of the group 1A harzburgites and group 1B xenoliths form distinct arrays of higher Cr# with respect to 1A lherzolites. In all the diagrams of Fig. 11, the sample scattering decreases when considering xenoliths from single localities.

5.5. Amphibole and phlogopite

Amphibole, pargasite, (Table 4, and web site http://www.terra.unimo.it/download/Petrografia/rivalenti/) is abundant only in group 1B samples of G. Gregores. Only one sample of Tres Lagos and two from Cerro del Mojon contain amphibole. At G. Gregores, amphibole may contain up to 0.15 wt% Cl. Laurora et al. (2001) distinguished the amphiboles of this locality into two

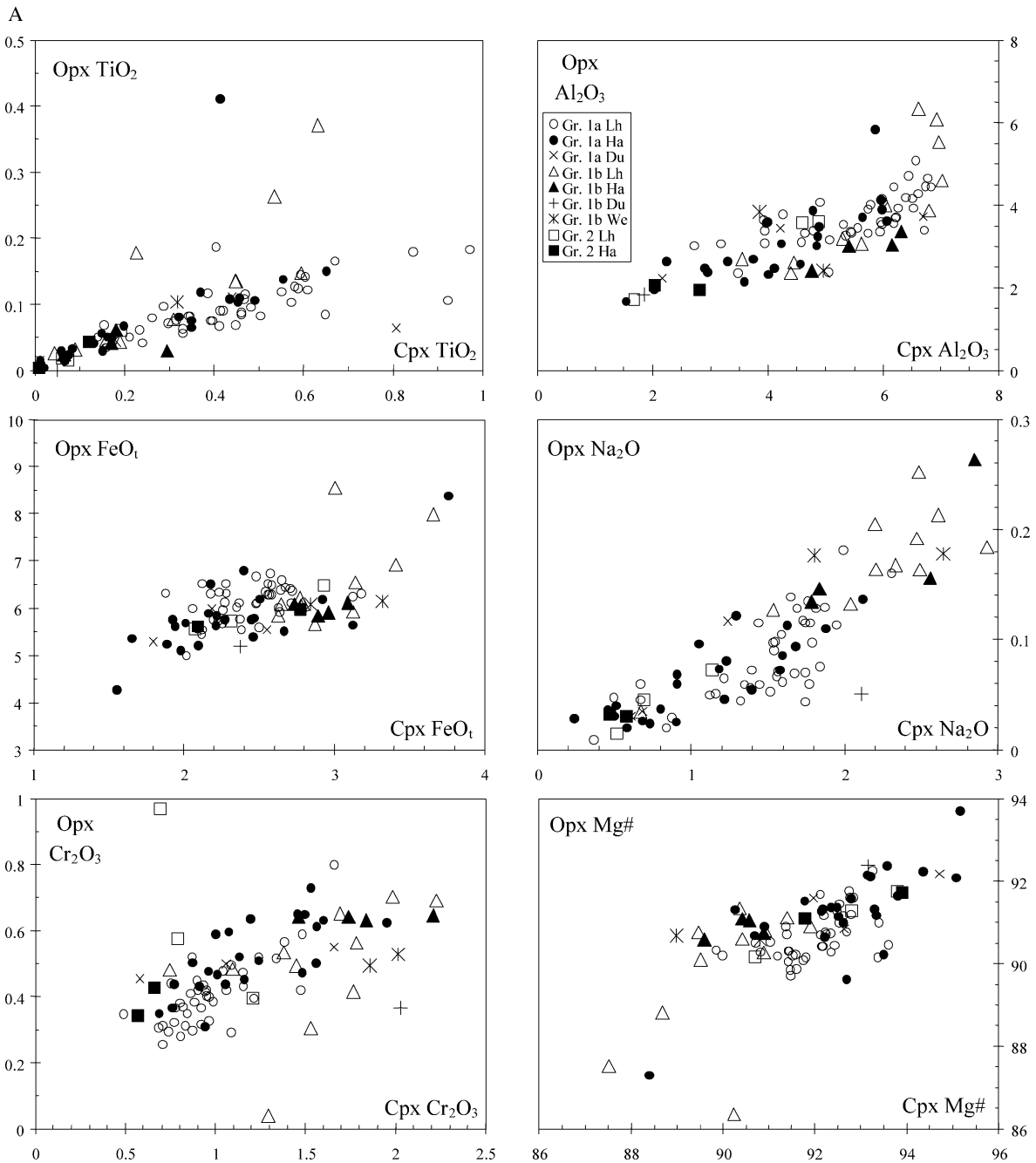

Fig. 8. Correlations of the major (A) and trace element concentrations and element ratios (B) between ortho and clinopyroxene.

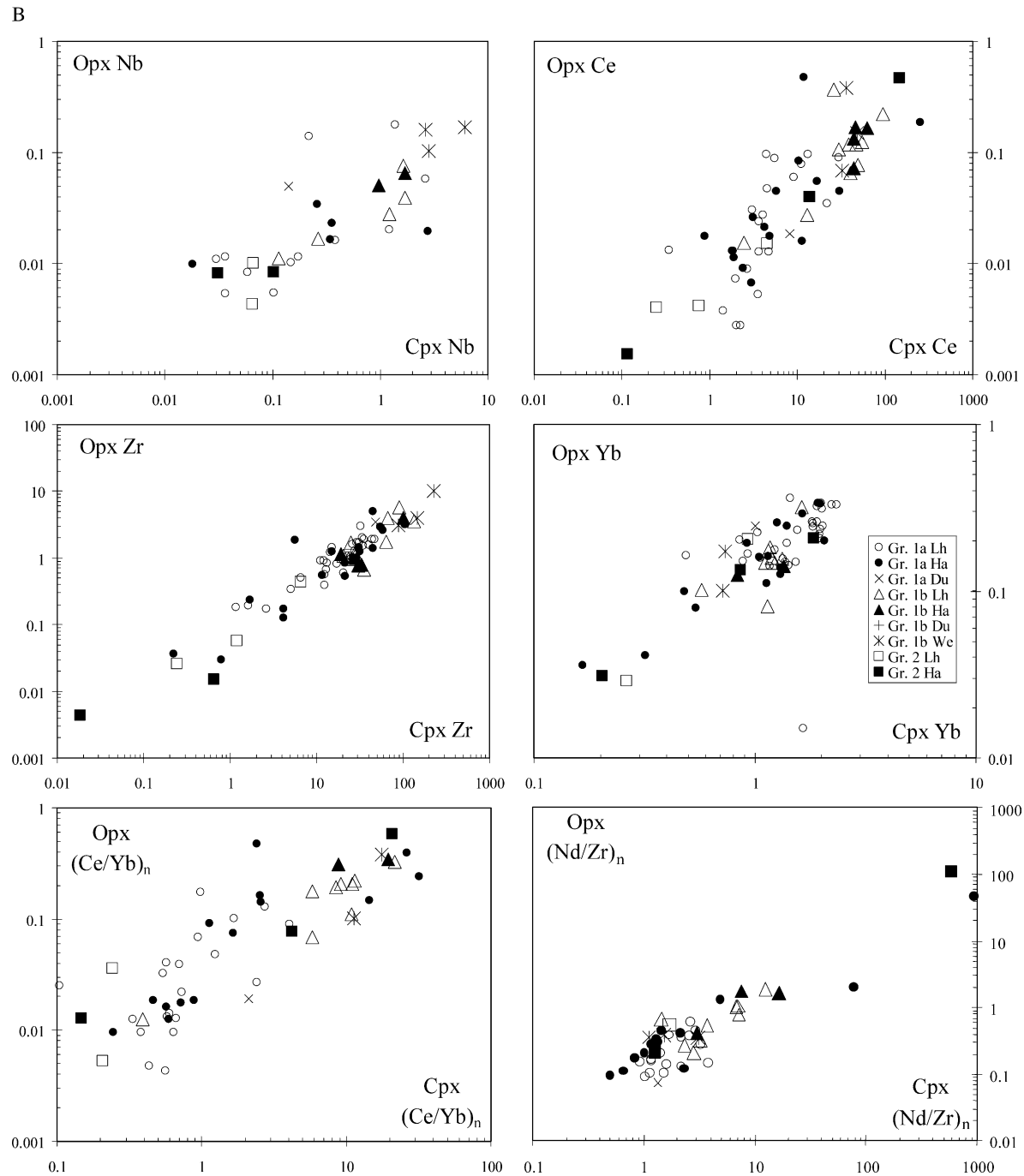

Fig. 8 (*continued*)

groups based on the TiO_2 concentration, ranging between 0.34–1.0 wt% and 3.28–3.90 wt%, respectively. The low-Ti amphiboles have higher Mg# (0.90 ± 0.004), Cr_2O_3 (2.18 ± 0.33 wt%) and (La/Yb)*n* (11.15 ± 3.55) than the high TiO_2 ones (0.85 ± 0.02, 1.12 ± 0.36 wt% and 6.19 ± 2.22, respectively). Extended trace element profiles (Fig. 12) show that, in the high-Ti amphiboles, Ba is enriched with respect to Th and U, (Nb,Ta)/La ratios are high, Zr and Hf are depleted with respect to REE and Ti exhibits positive anomalies. The low-Ti amphiboles have comparatively higher positive Nb spikes and may display a negative Ti anomaly. The amphibole REE patterns are similar to those of the coexisting clinopyroxene. The $^{amph/cpx}D$'s are comparable with those observed in other occurrences (Fig. 12) and show that amphibole preferentially fractionates Nb, Ta, Ti, Sr and Ba (the latter being below the detection limit in most clinopyroxenes). Zr and Hf preference for amphibole or clinopyroxene is unclear. The $^{amph/cpx}D_{REE}$ is close to unity, except in a few cases (GG92 and GG33) where

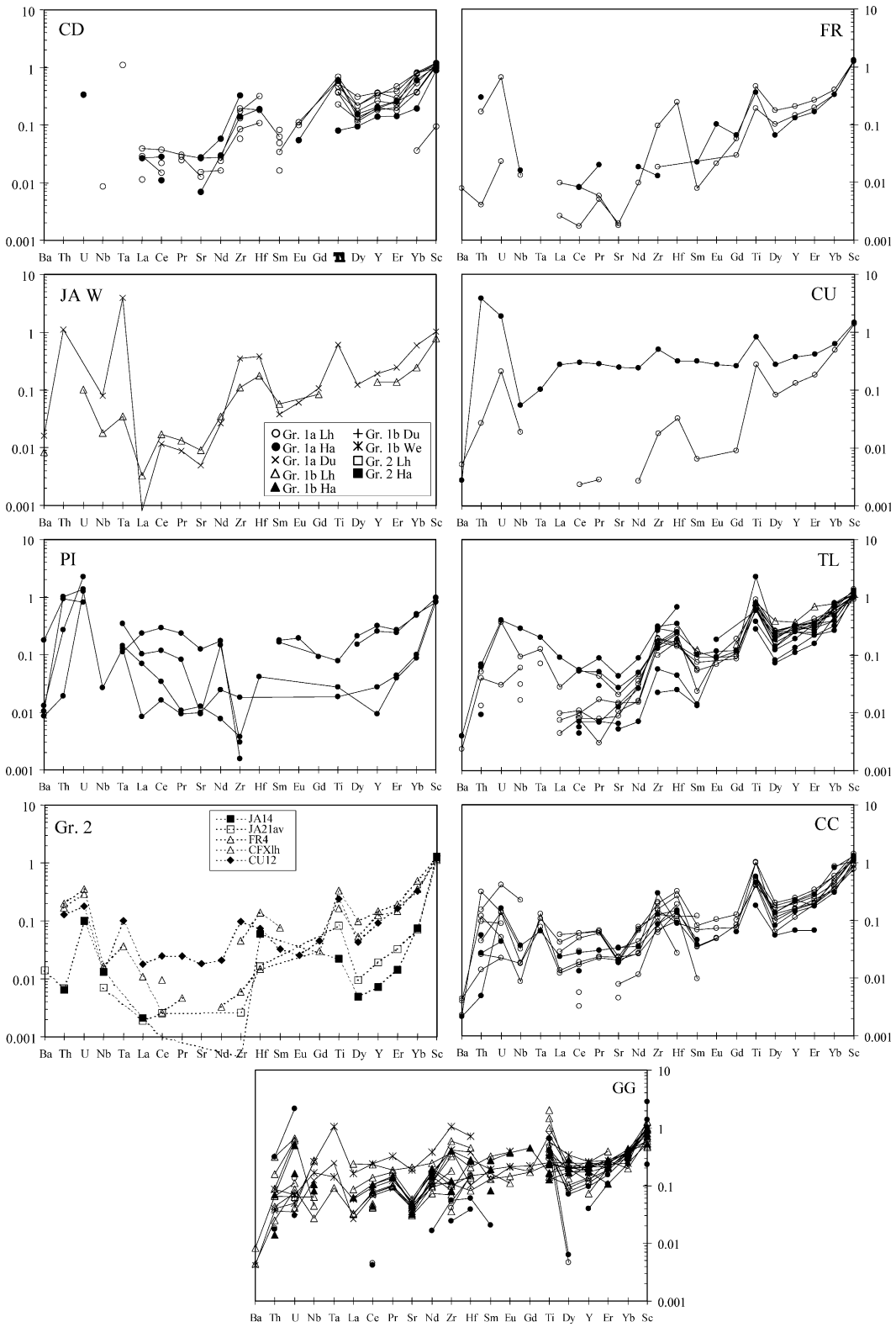

Fig. 9. Primitive mantle (Hofmann, 1988)—normalised trace element patterns of orthopyroxene.

REE are preferentially hosted in clinopyroxene. Amphibole at C. del Mojon is similar to those of G. Gregores, whereas at Tres Lagos amphibole is, like its coexisting clinopyroxene, LREE-depleted.

Phlogopite is the major host for Rb, Ba and K and together with amphibole, for Nb and Ti (see extended trace element pattern in Laurora et al., 2001). Its REE concentration is very low, close or below the detection limit.

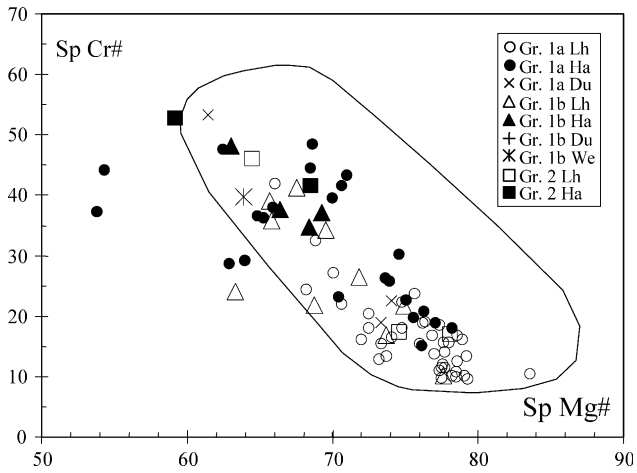

Fig. 10. Covariation of the Cr# [mole Cr/(Cr + Al + Fe^{+3})] and Mg# [mole Mg/(Mg + Fe^{+2})] values in spinel compared with the variation array in abyssal peridotites (Hellebrand et al., 2002).

5.6. Apatite

It has been found, not in connection with glass veins and pockets, only at Paso de los Indios and G. Gregores (Table 1). According to Laurora et al. (2001) at G. Gregores, it is a Cl-apatite (Cl 1.8–2.1 wt%; F 0.34–0.55 wt%) having very high LREE concentrations (La_n = 2877–3814), highly fractionated REE pattern [(La/Yb)n = 204–265], high Sr and Ba concentrations (8270–10813 ppm and 350–412 ppm, respectively), low Nb and Zr concentrations and Ta and Hf below the detection limit.

6. Temperature and pressure

Temperature estimates according to Brey and Köhler (1990) are reported in Table 2. Although the temperatures of the group 1A and B largely overlap, the highest values are found in the second and may be as high as 1200 °C. Temperatures below 900 °C are very rare (only five harzburgites). The equilibrium temperatures of the 1B xenoliths exceed the upper limit for amphibole stability, which is consistent with the fact that at G. Gregores amphibole is an unstable phase undergoing disequilibrium melting. On the other hand, this also indicated that the thermal-decompression event that induced amphibole instability was able to re-equilibrate the pyroxenes. If so, it is possible that also in the other localities pyroxenes were variably re-equilibrated during the thermal increase predating or accompanying xenolith entraining into the basalts and that the thermal characteristics of the various localities largely record overprinting by this late event.

Because of the spinel-facies, pressure conditions are difficult to constrain. Pressure calculated using the Mercier (1980) geobarometers results in similar ranges (1–2.5 GPa)

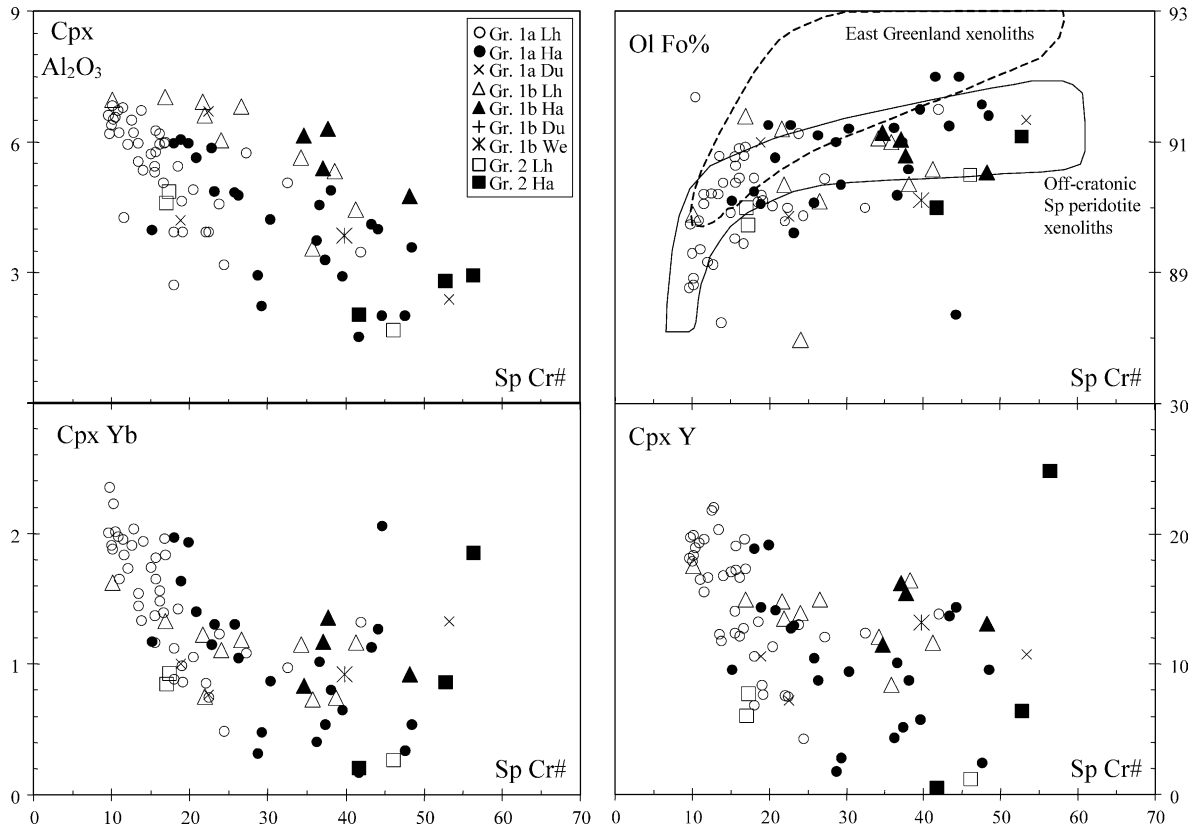

Fig. 11. Variation of the Fo concentration in olivine and the Al_2O_3 (wt%), Y and Yb (ppm) concentration in clinopyroxenes with respect to the Cr# value of the coexisting spinel. The fields of the East Greenland and off-cratonic spinel-peridotite xenolits are from Ionov et al. (2002).

Table 4
Selected amphibole major and trace element composition of Patagonian xenoliths

	Cerro del Mojon		Gobernador Gregores				Tres Lagos
	JAW40	JAW41	GG92	GG104	GG73	GG33	TL72
Group	1b	1b	1b	1b	1b	1b	1b
Lithotype	Lh	Lh	Lh	Lh	Lh	We	Lh
(Wt%)							
SiO_2	43.72	43.10	42.93	43.37	44.53	43.78	42.97
TiO_2	1.67	1.94	3.40	0.37	0.34	3.91	3.16
Al_2O_3	13.38	13.36	14.29	13.63	13.32	13.99	15.34
FeO_{tot}	3.96	3.79	5.57	3.60	3.76	4.32	4.46
MnO	0.04	0.07	0.06	0.06	0.07	0.07	0.06
MgO	18.34	17.74	16.10	18.48	18.26	16.43	15.55
CaO	11.17	10.87	9.66	10.93	10.21	9.06	10.67
Na_2O	3.31	3.00	3.43	3.46	3.48	3.59	2.62
K_2O	0.86	0.80	1.67	1.50	1.28	1.25	2.17
Cr_2O_3	1.77	1.65	0.78	2.44	2.57	1.49	0.94
Cl			0.02	0.07	0.08	0.02	
(ppm)							
Rb		3.06	5.9	5.5	4.9	3.3	17
Ba	92.86	93.57	222	427	204	125	268
Th		0.14	0.22	1.2	0.57	0.066	
U		0.15	0.066	0.40	0.25	0.050	0.01
Nb	10.10	10.61	23	295	250	40	4.6
Ta			1.2	10	4.8	2.1	
La	6.09	5.75	9.2	22.8	17.8	4.8	0.97
Ce	17.92	18.36	32.7	64.9	58.2	16.9	4.3
Pb		0.63	0.59	1.2	1.4	0.55	
Pr		2.95	5.3	9.0	8.9	3.4	0.95
Sr	417.85	401.08	612	659	667	531	185
Nd	13.00	13.50	24.4	36.5	37.4	20.3	5.8
Zr	39.56	38.85	83	81	44	68	30
Hf		1.31	2.2	0.18	0.21	1.6	0.92
Sm	3.27	3.38	7.0	8.8	10.0	6.9	2.42
Eu	1.18	1.27	2.08	2.30	2.60	2.21	0.94
Gd	2.89	3.48	5.0	5.0	5.4	5.8	3.1
Dy	2.69	2.85	2.92	2.95	3.5	3.7	3.4
Y	15.03	14.91	12.3	12.4	14.5	13.2	22
Er	1.39	1.39	1.09	1.16	1.42	1.25	1.95
Yb	1.13	1.09	0.74	0.88	0.98	0.81	1.85
Sc	45.50	50.39	26	37	46	22	40

Blank values, below detection limit (see text).

for ortho and clinopyroxene and does not show clear regional variations. The Ca-in-olivine geobarometer of Köhler and Brey (1990) gives inconsistent results, perhaps because the available electron microprobe Ca determination in olivine is not precise enough.

7. Geochemical evidence for partial melting

The bulk-rock and clinopyroxene trace element profiles are compared with the results of batch and fractional non-modal melting models of a primitive mantle source (Hofmann, 1988) in Figs. 4 and 6, respectively. Parameters used in modelling are in the figure captions. Only the group 1A profiles resemble the models in their HREE, Y and Ti variations. As observed in many other xenolith occurrences (Takazawa et al., 2000; Xu et al., 2000; Grégoire et al., 2001; Hellebrand et al., 2002) all the other elements diverge from the melting models towards higher concentrations. Divergence increases with increasing element incompatibility. While in bulk-rock, these enrichments may be due to glass, their occurrence in clinopyroxene indicates they are a feature related with mantle processes. The relationship with the melting models is specifically illustrated in Fig. 13 for selected elements, showing that HREE (and Ti, see the Fig. 13 caption) fit model variations induced by fractional melting up to ~25% melting. While LREE (exemplified by Ce) and HFSE (Zr) do not. Melting range up to ~25% results also from the variation of the Cr# number of spinel and its correlation with the Yb concentration in clinopyroxene (Hellebrand et al., 2001).

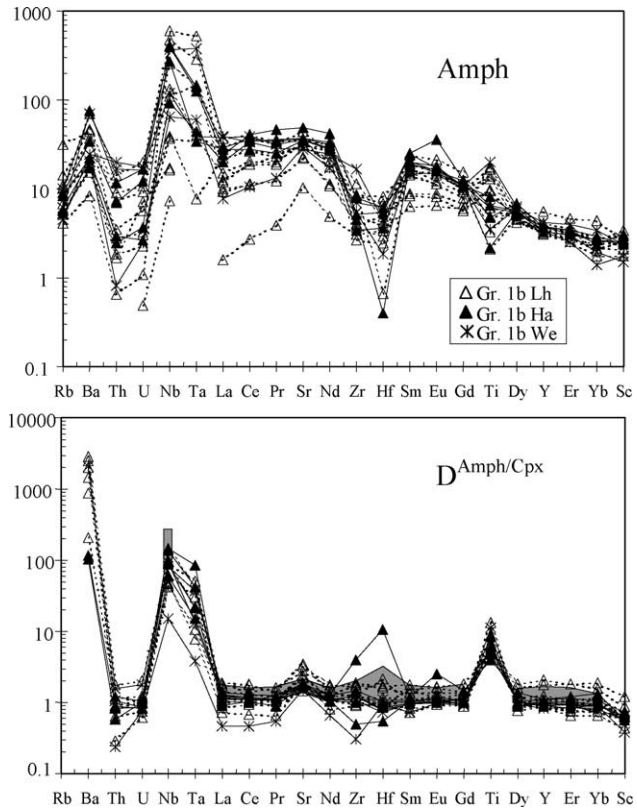

Fig. 12. (A) Primitive mantle (Hofmann, 1988)—normalised trace element profiles of amphibole. (B) Amphibole/clinopyroxene trace element partitioning compared with West Eifel data (shaded field, Witt-Eickshen and Harte, 1994).

None of the group 1B xenoliths and their clinopyroxenes fit model melting trends. The HREE profile of the group 2 clinopyroxenes may be explained by fractional melting up to ~20% (Ja14), but all clearly show enrichment of LILE and REE in the range La–Sm or Gd in sample Cu12.

8. Potential melt composition

The composition of the potential melt/fluid in equilibrium with clinopyroxene may be estimated using its solid/melt partition coefficients (Grégoire et al., 2000; Moine et al., 2001).

By using the partition coefficients of Hart and Dunn (1993), the potential melts in equilibrium with the 1A, LREE-depleted, clinopyroxenes are very similar, as far as their Nb depletion and LILE and REE patterns, to the Patagonia arc magmas (Hickey et al., 1986; Stern and Kilian, 1996), from which they differ for a slightly negative Zr and Hf anomaly (Fig. 14). In the southern region, however, the Nb depletion becomes more tenuous eastwards (e.g. at C. Cuadrado and G. Gregores) and the trace element profile becomes similar to that of E-MORB or backarc Patagonia basalts (Gorring and Kay, 2001). Furthermore, in the 1A potential melts of all the southern localities except Cumbres, the Nb depletion disappears at increasing trace element concentration (i.e. in the melts calculated from LREE-enriched pyroxenes). Incompatible trace element enrichment is also paralleled by an increase in the REE fractionation, variation of the (Th/U)n ratio from sub-chondritic to Th-enriched and attenuation of the Zr and Hf anomalies. These variations do not occur in the northern region, where Nb depletion is also maintained in the incompatible element-enriched melts and only two cases at Paso de los Indios (Pi18 and Pi52) do not show Nb depletion.

Potential melts estimated by using clinopyroxene partition coefficients for hydrous basaltic liquids (Green et al., 2000) improve the similarity with arc magmas, but still preserve the eastwards variation to melts more similar to E-MORB. This is exemplified in Fig. 14 for the Cumbres and C. Cuadrado localities, showing that the melts estimated by using the Green et al. (2000) data set have lower concentration and higher REE fractionation, a positive Sr spike, attenuated Zr, Hf and Ti anomalies, but do not alter the La–Nb relationship with respect to melts estimated from Hart and Dunn (1993) partition coefficients.

In the potential melts from the 1B xenoliths, increasing incompatible trace element concentration goes together with a relatively narrow range of REE fractionation (Fig. 14) and with very large variations of the HFSE anomalies (at G. Gregores, Zr*/Zr = 0.6–7.8; Hf*/Hf = 2.8–67.6, Ti*/Ti = 1.8–27.5), that were shown in the G. Gregores clinopyroxenes to be poorly dependent on the variations of the REE concentration, but highly controlled by variation of the HFSE element (Fig. 7). Even more marked HFSE depletions occur at Paso de los Indios (Zr*/Zr = 393; Hf*/Hf = 397 and Ti*/Ti = 200 in Pi29; Ti*/Ti = 749 in Pi16), the easternmost occurrence of the northern region having group 1 xenoliths. These strong HFSE fractionations and LREE enrichments are often considered typical of carbonatite metasomatism (Yaxley et al., 1991; Rudnick et al., 1993; Hauri et al., 1993) and this was the interpretation of Gorring and Kay (2000) for G. Gregores. However, in other xenolith occurrences similar characteristics where attributed to alkaline silicate melts and/or reactive porous flow (Chalot-Prat and Boullier, 1997; Grégoire et al., 2000; Ionov et al., 2002) and, for G. Gregores, Laurora et al. (2001) emphasise metasomatism operated by a hydrous silicate melt having an imprint from a subducted slab.

9. Regional variations

Regional variations of geochemical features are shown in Figs. 4, 6, 9 and 14 where the localities are arranged from West to East and distinguished in the regions North and South of longitude 46.30°S. Note that the two regions represent backarc segments of different size and the localities C. Cuadrado in the South and C. del Mojon and C. Chenques in the North have about the same longitude (Fig. 1). A striking regional feature is the presence of LREE-depleted bulk-rock and clinopyroxenes in all the localities

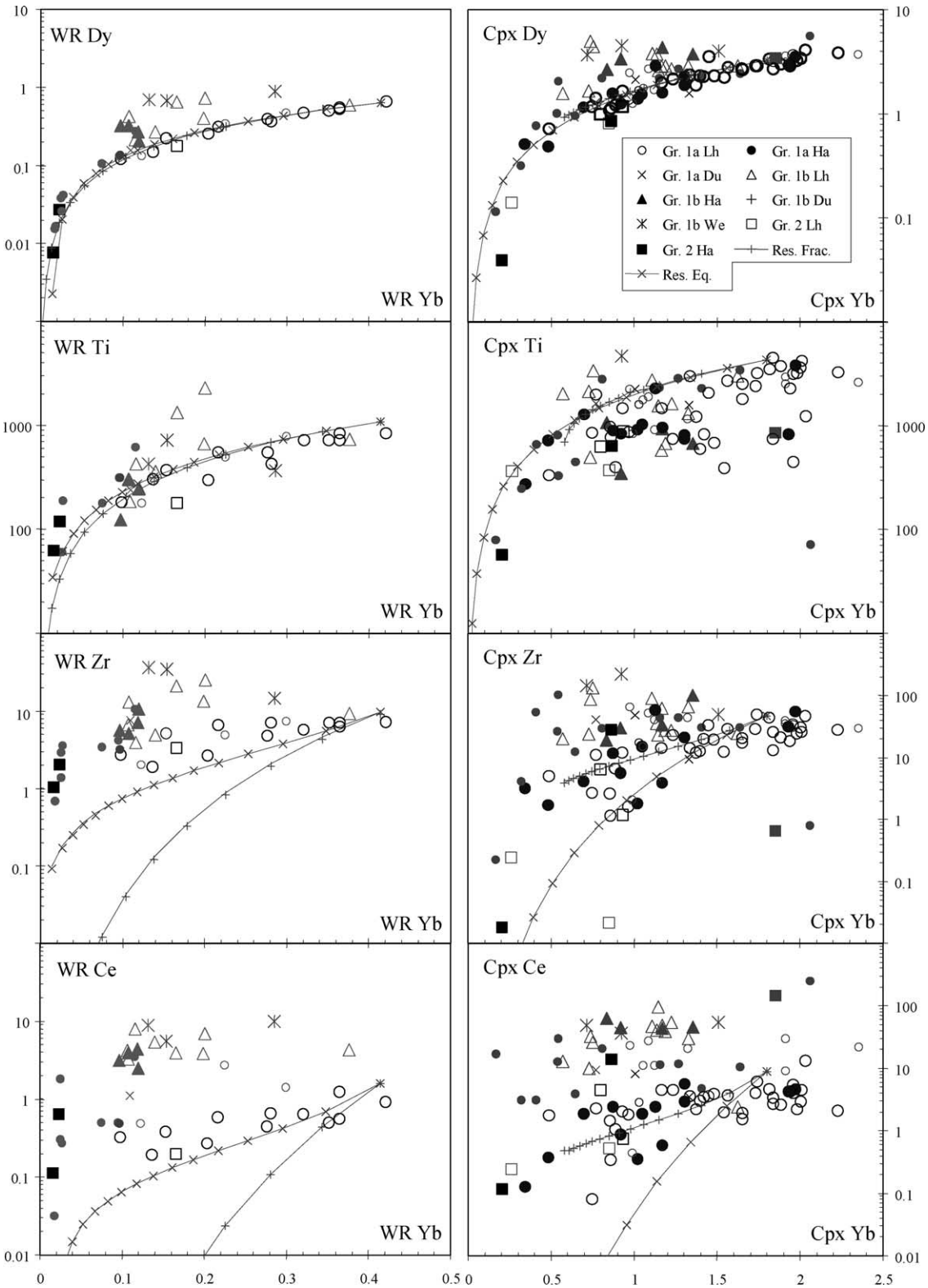

Fig. 13. Variations of Dy, Ti, Zr and Ce (ppm) with respect to Yb (ppm) in bulk-rock and clinopyroxene compared with fractional and equilibrium non-modal melting trends of clinopyroxene in a primitive mantle (Hofmann, 1988) source. Ticks on the lines are 2% melting steps. Parameters in the models are in the Fig. 4 caption. Dark black symbols, LREE-depleted bulk-rocks and clinopyroxenes; gray symbols, LREE-enriched bulk-rocks and clinopyroxenes. The lower Yb concentration in the clinopyroxene estimated to be in equilibrium with primitive mantle with respect to the analytical data is dependent on the primitive mantle composition and on the equations used in the model. The difference would disappear by using the Sun and McDonough (1989) primitive mantle composition and the melting equations of Norman (1998) (see also Grégoire et al., 2001), who neglects the effects of the other phases coexisting with clinopyroxene during melting.

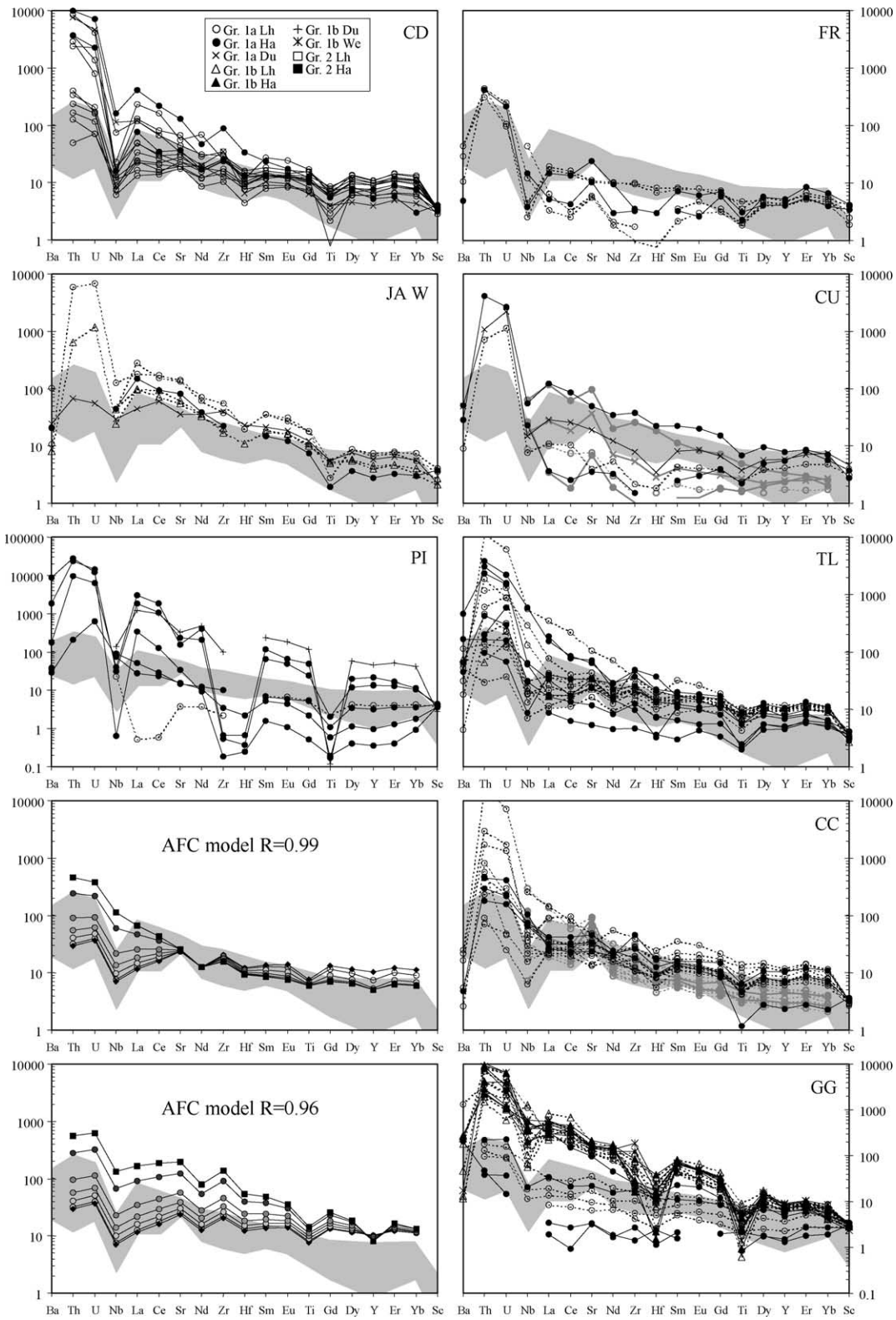

Fig. 14. Potential melts in equilibrium with the group 1 clinopyroxenes (cpx/D). The composition range of the Patagonia arc basalts and adakites (data sources: Hickey et al., 1986; Stern and Kilian, 1996) reported for comparison is represented by the shaded field. Partition coefficients are from Hart and Dunn (1993) Partition coefficients for Th and U are from Foley et al. (2001). Potential melts calculated by using the D set of Green et al. (2000) for hydrous basalts are reported in gray in the C. Cuadrado and Cumbres diagrams. With respect to those calculated from Hart and Dunn (1993) data, they have lower concentration and higher fractionation of REE, a positive Sr anomaly and attenuated Ti, Zr, and Hf anomalies. The two diagrams on the left column, bottom, illustrate the results of an AFC model assuming $R = 0.98$ and 0.96 (R, the mass of peridotite with which the melt re-equilibrates/the mass of peridotite with added reaction products) Model parameters: ambient peridotite, residuum from 15% non-modal batch melting of primitive mantle (ppm Th 0.0007, U 0.0001, Nb 0.004,

of the southern region and (within the limit of representativity of the present samples) their rarity in the northern region, where they occur abundantly only at C. Chenques, but are recorded only in one sample at Paso de los Indios. This is especially evident if localities at approximately the same longitude are considered (e.g. from South to North, C. Cuadrado, C. Chenques and C. del Mojon or G. Gregores, Paso de los Indios and Estancia Alvarez). Along the second xenolith array, in addition to the decrease of LREE-depleted clinopyroxene abundance, there is also a northward increase in group 2 xenoliths, absent at G. Gregores, present at Paso de los Indios and dominant at Estancia Alvarez. Other important regional variations concern the Nb/La ratio, that increases eastwards in the LREE-depleted clinopyroxenes and their potential melts of the southern region and remains constantly very low in the northern region. In both regions, there is also an eastwards increase in xenoliths having highly fractionated, LREE-enriched, clinopyroxene patterns and stronger negative Zr, Hf and Ti anomalies, as is clear considering the 1B xenoliths of G. Gregores and the 1A xenoliths of Paso de los Indios, in the southern and northern regions, respectively.

10. Discussion

Points discussed next are: (1) the reason of the overlapping major element composition in the 1A harzburgitic and lherzolitic clinopyroxenes; (2) the process inducing enrichment of highly incompatible elements in xenoliths recording melting and the relationship between the enriching and melting processes; (3) the metasomatic process in the 1A LREE-enriched and in the 1B clinopyroxenes, and the nature and provenance of the metasomatic agent.

10.1. The relationship between the group 1A lherzolites and harzburgites—A model and a speculative mantle stratigraphy

Kelemen (1995) argued that reaction between ascending mantle melts (hydrous picritic liquids) and mantle peridotite may explain the genesis of high-Mg andesites and that the percolation-reaction process leads to orthopyroxene enrichment in the mantle. Based on Kelemen's strategy, we present a model for explaining the major element characteristics of the 1A lherzolitic and harzburgitic clinopyroxenes, their HREE and Ti consistency with melting processes and the geochemistry of the other elements.

Since mantle-derived melts preserve a 'memory' of their provenance in their trace element characteristics, we assume infiltration of a hydrous, silica-rich melt (Y in Fig. 15A), as suggested by the localities where potential melts resemble arc magmas. We also assume infiltration into an anhydrous mantle region close, but below, its solidus temperature, as suggested by Kay (2002), who concluded that the Patagonia mantle was close to melting since Mesozoic. The composition of the equilibrium melt of the peridotite modified by the slab hydrous component is at X (consistent with Kushiro (1969) experiments on hydrous peridotite system at 2 GPa) (Fig. 15A), at a temperature lower than that of the anhydrous solidus. Under hypersolidus conditions, the composition of the added component would rapidly evolve to that of this minimum-T melt by reacting with the peridotite, as suggested by the experimental work of Carroll and Wyllie (1989); Rapp et al. (1999). Ambient temperature in excess of that of the minimum-T melt X would result in increasing melt mass of constant composition until consumption of one of the reacting phases. In the specific case, the excess temperature would be compensated by a higher (endothermic) dissolution rate of olivine, in peritectic relationship with Y and consumption of clinopyroxene in amounts proportional to the temperature excess in order to maintain constant the melt composition at X. The modal variations in a mantle assumed to be initially lherzolitic would consist in a decrease in olivine and clinopyroxene and increase in orthopyroxene (Fig. 15A), that is quite different from the closed-system melting trend (Fig. 15A), leading also to harzburgite, but following a concomitant decreasing path for clinopyroxene and orthopyroxene. When melting occurs during reaction, a variety of residual peridotites are formed within the space limited by the melting and reaction vectors (Fig. 15A). These peridotites are in equilibrium with a melt of essentially constant composition, not withstanding the influence of other variables such as the effects of solid solutions and the water content of melt Y that controls the temperature of melt X (Green, 1973; Hirose and Kawamoto, 1995; Gaetani and Grove, 1998) and, therefore, the excess temperature. The observed largely overlapping major element composition range of the lherzolites and harzburgites silicate phases are thus easily explained because they could have equilibrated with a melt of variable mass and similar compositional range. The model may account also for the apparent consistency of the spinel composition with melting processes (Fig. 10). Equilibration of spinel with silica-rich melts induces a shift, proportional to the mass of the silicate melt, towards a Cr-richer composition (see the phase diagrams in Irvine, 1975, 1977). Being melt mass higher in the harzburgite than in the lherzolite region, more refractory spinel compositions are expected in the former.

When the ambient temperature falls below that of X, melts are no longer constrained by the X composition and

La 0.022, Ce 0.092, Sr 1.494, Nd 0.140, Zr 1.010, Hf 0.041, Sm 0.067, Eu 0.030, Ti 295.9, Gd 0.121, Dy 0.170, Y 1.552, Er 0.118, Yb 0.128); infiltrated melt: TL30 potential melt (ppm Th 2.371, U 0.736, Nb 4.310, La 7.072, Ce 25.992, Sr 425.75, Nd 14.889, Zr 200.594, Hf 3.297, Sm 5.334, Eu 2.059, Ti 8322.9, Gd 6.805, Dy 7.424, Y 41.299, Er 5.146, Yb 4.604. Partition coefficients as in Fig. 4. See text for further information.

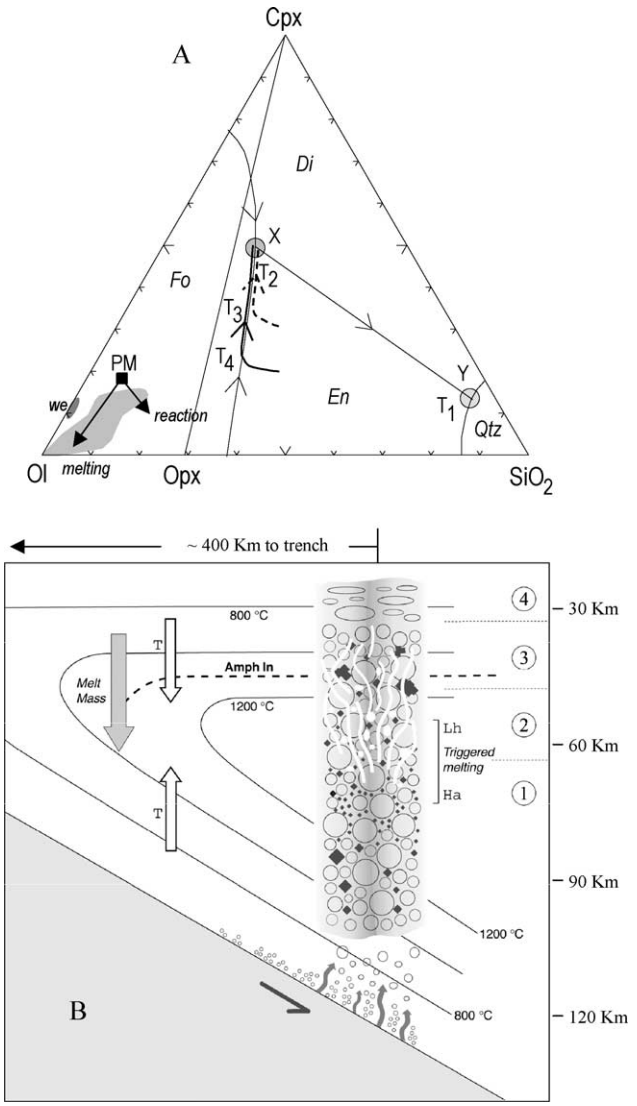

Fig. 15. (A) Pseudo-ternary Ol-Cpx-SiO_2 system at 2 GPa (Kushiro, 1969) illustrating the model proposed in the text. X is the pseudo-ternary hydrous minimum-T melt at temperature T_2. A hydrous, slab-derived, melt (Y, T_1) infiltrates the peridotites at temperatures T_4 and T_3 ($T_4 > T_3 > T_2 > T_1$), reacts with olivine forming orthopyroxene and moves towards X by absorbing clinopyroxene along the peritectic line orthopyroxene-olivine. The dashed and continuous arrows indicate the melt path at T_4 and T_3, respectively, showing that clinopyroxene resorption depends on the excess temperature with respect to T_2. The dashed field represents the xenolith modal composition and the two arrows from PM (primitive mantle) are melting and reaction vectors. (B) Cartoon of an arbitrary wedge section ~400 km distant from the trench, as could be Tres Lagos. Depth scale, implying a ~20° slab dip, is also arbitrary, and is meant to locate the melting zone in spinel-facies mantle. Infiltration of a slab-derived component (dashed circles and black arrows) triggers melting of the mantle wedge in the region of thermal inversion (origin of the white veins and the white circles), producing harzburgites under increasing T and melt mass (region 1) and lherzolites under decreasing T and melt mass (region 2). Region 3 is below the peridotite solidus and undergoes reactive porous flow of region 1 and 2-derived melts. Amphibole (black squares) is a reaction product when its stability conditions are crossed. Region 4 is the uppermost, relatively cold, lithosphere undergoing infiltration and chromatographic enrichment by the residual percolating melts. Black diamonds, clinopyroxene. Circles simulate olivine and granular texture, turning to elipses in the porphyroclastc peridotites of region 4.

reaction of the peridotite with the infiltrated melt will decrease the mass and vary the composition of the latter until equilibrium with the peridotite is reached. Hydrous phases would crystallise by reaction when the T, P conditions would permit it. Ephemeral, residual melts may percolate the upper, colder regions of the lithospheric mantle resulting in chromatographic element fractionation and diffusion-related enrichment of the matrix phases, without reactions or re-crystallisation.

This model works also if the infiltrated component is a hydrous basalt, as could be for the localities, like G. Gregores, where the potential melts resemble E-MORB more than arc magmas. As illustrated by the diagrams II and III in Kelemen (1995) Fig. 3 (see also Kelemen et al., 1998), infiltration would ultimately lead to an orthopyroxene increase in the infiltrated mantle and to silica-enriched derivative melts, but the peridotite modal evolution would include stages where both pyroxenes are dissolved and olivine is enriched. This is consistent with the high modal olivine concentration observed in some harzburgites (see Section 4). Infiltration of alkaline melts under spinel-facies pressure conditions and at decreasing melt mass would induce orthopyroxene dissolution and a trend towards wehrlite until the residual melt is sufficiently silica-enriched to be in equilibrium with orthopyroxene (Hirschmann et al., 1998).

The process illustrated in the model would be especially efficient in convergent plate regions. Because of the inverted geothermal structure of convergent zones (Davies and Stevenson, 1992), slab-derived, hydrous, silica-rich melts would be heated while percolating the mantle wedge, thus becoming extremely reactive against the ambient peridotite. Kelemen (1995) calculated that 100 g of silicic melt heated from 900 to 1200 °C has the thermal energy to dissolve 100 g peridotite even at constant pressure. A harzburgite region (1 in Fig. 15B) may occur at the thermal maximum of the wedge and it is overlain, when temperature decreases but is still above the solidus, by lherzolites (2 in Fig. 15B). The latter region may interact with melts derived from region 1, that have the composition of melt X and are, therefore, not so strongly reactive against peridotite. Region 2 in turn fades into a region (3 in Fig. 15B) dominated by reactive porous flow under decreasing melt mass below the solidus temperature. The uppermost member (4 in Fig. 15B) represents the shallower and colder mantle where no reactions occur.

10.2. Trace element behaviour predicted by the model

Trace element concentration in peridotites of regions 1 and 2 is function of (i) the composition of the protolith before infiltration and of the added material and (ii) the amount of melt formed and the melt extraction rate. Elements depleted in the added component are dominantly controlled by the peridotite composition. The process leading to harzburgites induces a mantle region of high

porosity (Kelemen et al., 1995) with respect to the lherzolite region and, therefore, facilitates melt flow and extraction processes. The result is that trace elements variations in the residual peridotite resemble those induced by closed-system fractional melting and melt extraction. On the contrary, the concentration in the melt and peridotite mineral phases of elements highly enriched in the added component would significantly deviate from geochemical trends typical of closed-system melting processes. Vernières et al. (1997) modelled trace elements in peridotites undergoing melting during infiltration of an OIB component. They show that bulk-rock (and hence clinopyroxene) become depleted in incompatible trace elements but are relatively enriched in the elements concentrated in the OIB, so that LREE/HREE is close to 1. The geochemical features of the LREE-depleted group 1A harzburgites and lherzolites are, therefore, consistent with region 1 and 2, respectively. In these xenoliths, Y, HREE and Ti concentrations, that follow variations typical of fractional melting, behave like elements highly depleted in the added component. Deviations from fractional melting increase with increasing element incompatibility, thus suggesting complementary increases for these elements in the added component. Depletions of HREE and Y in the added component are consistent with the presence of garnet in its source (granulite- or eclogite-facies slab, or garnet-facies mantle). Depletion of Ti is consistent with the presence of a phase, like rutile, fractionating Ti in the source.

Infiltration under decreasing melt mass of the region 1 and 2—derived melts into region 3 leads to an increase in the incompatible elements both in the melt and reacting peridotite (Kelemen, 1995). The results of reactive porous flow under decreasing melts mass are documented in several xenolith studies (Bedini et al., 1997; Ionov et al., 2002; Raffone et al., 2002). Main factors controlling the trace element enrichment in the peridotite are the amount and composition of the infiltrated melt, porosity, reaction rates and melt/peridotite partition coeffients. In the absence of phases able to fractionate HFSE, percolation into an anhydrous peridotite (corresponding with the 1A LREE-enriched xenoliths) should induce enrichment of all the incompatible elements, but not HFSE-REE fractionation. However, this happens for Nb in the LREE-enriched group 1A clinopyroxenes (see next chapter). When the percolating melt crosses the T, P conditions limiting amphibole stability (as, for example, in the 1B xenoliths at G. Gregores), its crystallisation induces important decoupling between the HFSE preferentially partitioned into this phase (Nb, Ta and Ti) and REE.

Infiltration into the low-T region 4 of the last, ephemeral melts is dominated by element diffusion, chromatographic element fractionation (Navon and Stolper, 1987; Vernières et al., 1997) and preservation of the mode predating infiltration, as observed in the group 2 xenoliths. The group 2 clinopyroxenes at Cumbres and Fraile are LILE and LREE-enriched and have negative Nb anomalies, indicating complementary geochemical characteristics of the metasomatic agent. Those of C. del Mojon and one of Paso de los Indios (Pi41) do not have an appreciable negative Nb anomaly.

10.3. Provenance of the melt infiltrating region 3

1A xenoliths. At Tres Lagos and C. Cuadrado and possibly Fraile, the Nb depletion relative to LILE and La in the group 1A, potential melts progressively disappears at increasing incompatible element concentrations, whereas it is preserved in other locals (e.g. all those of the northern region and Cumbres). This may suggest that two different melts (one derived from region 1 and 2 and an exotic melt) infiltrated the mantle of the former localities and only one (region 1 and 2—derived) the latter ones. We have tested the hypothesis that in all cases, the infiltrated melt derived from the 1 or 2 regions using an AFC model (DePaolo, 1981). Since the melts were in equilibrium with peridotite in regions 1 and 2, they would not be strongly reactive against peridotite in region 3. Reactions are expected to originate only by disequilibrium peridotite-melt induced by decreasing T, P gradient and by that caused by the variable composition (suggested by the group 2 xenoliths) in the mantle segment undergoing percolation. For this reason, we assume in the model complete re-equilibration with the peridotite and decreasing porosity. These two factors are approximated by high R values (R, the mass of peridotite with which the melt re-equilibrates/the mass of peridotite with added reaction products) and ^{bulk}D consistent with the peridotite mode. The composition of the mantle segment before percolation is assumed to be that of a depleted lherzolite (residue from 15% melting of primitive mantle, Hofmann, 1988) and the infiltrated component is assumed to be similar to the potential melt in equilibrium with the TL30 clinopyroxene that is Nb-depleted. The results are illustrated in Fig. 14 (other parameters are in the figure caption). The Tres Lagos and C. Cuadrado variation range can be successfully approximated assuming very high R values (0.98–0.99) and decreasing melt mass down to 5% of the initial volume. Lower R values (e.g. 0.90–0.95) fractionate LILE and LREE from HREE, but not HFSE from REE, resulting in a variation range similar to that of C. Chenques. These results indicate that, when amphibole is absent, there is no need for infiltration of an exotic melt in order to explain the geochemical characteristics of the region 3 xenoliths, that may be accounted for by infiltration of the regions 1 and 2 melts under different porosity regimes, lower at Tres Lagos and C. Cuadrado with respect to C. Chenques.

1B xenoliths. Infiltration of melts derived from the 1 and 2 regions into region 3 is more difficult to assess when amphibole occurs as a reaction product in the 1B xenoliths. Considering the G. Gregores locality, where 1B xenoliths are more abundant, a link between the 1A and B xenoliths is suggested by the diagrams of Fig. 7, where the peak in the variation trends is concomitant with the amphibole entry

in the peridotite assemblage. However, the presence, although rare (only three samples) of wehrlites, formed by orthopyroxene dissolution and clinopyroxene crystallisation, may not support infiltration into region 3 of region 1 or 2-derived melts, because our model predicts these latter to be silica-saturated. Therefore, either the 1B xenoliths derive from a mantle region percolated by exotic melts, or keeping infiltration of the melts derived from the 1 or 2 regions, wehrlites cannot be an early reaction product, but need to originate from other processes during melt percolation.

One of the effect of infiltration of a silicate melt is to induce, both in bulk-rock and mineral phases, a decrease of the Mg# value dependent on the melt/peridotite ratio (Xu et al., 1998). Consistent with silicate melt infiltration, the clinopyroxenes of the 1B xenoliths at G. Gregores have lower Mg# values than the respective 1A, but the lowest Mg# values do not occur in wehrlites (Table 2 and Fig. 5), thus indicating they cannot be a reaction product at the base of the region 3 mantle. Furthermore, the clinopyroxene composition and HFSE anomalies of the wehrlites are in the range of the 1B lherzolites and harzburgites (Figs. 5–7), suggesting a control by the same processes and components. A possible process for explaining these features is unmixing of a small volume of an undersaturated melt from the silicate melt during its percolation, as proposed elsewhere by Zanetti et al. (1999); Raffone et al. (2002). Unmixing could be favoured by the presence of CO_2 (as suggested by the CO_2 abundance in fluid inclusions; Gorring and Kay, 2000, and our unpublished observations), and enhanced by Cl (abundantly occurring in apatite and amphiboles). Experimental evidences indicate that even small amounts of NaCl enhance liquid immiscibility in the H_2O–NaCl–CO_2 system (Popp and Frantz, 1990).

If melt umixing occurred, then also at G. Gregores the metasomatic component in region 3 may originate from regions 1 and 2. As emphasised by Laurora et al. (2001), amphibole crystallisation, that occurred when the thermal conditions for the stability of this phase were reached, and its compositional variations consequent to percolation may account for most of the observed trace element variations, including HFSE (Tiepolo et al., 2000, 2001). A weak point in this possibility (and indeed in any other possibility, such as infiltration of a carbonatite component) is the decoupling of the Zr, Hf behaviour with respect to REE (see Fig. 7) that is not supported by experimental data available at present. Although not specifically referred to Zr and Hf, a possible explanation is provided by the results of Vannucci et al. (1998), who observe that silica enrichment in melts (that in the present case could occur during reactive porous flow at decreasing melt mass) induces an increase in the REE partition coefficients, but leaves those of HFSE unchanged.

10.4. Nature of the metasomatic agent and its regional variations

Slab-derived components are generally believed to induce Na_2O, LILE and LREE enrichment and Nb depletion in the metasomatised mantle (Kepezhinskas et al., 1995; Ewart et al., 1998; Churikova et al., 2001; Grégoire et al., 2001). Such a slab signature is common in the Patagonia xenoliths and the interaction with slab-derived components is further supported by the similarity of the potential melts calculated from the 1A, LREE-depleted, clinopyroxenes with the arc magma compositions. It has been shown, however, that one of the typical slab features, the Nb depletion, fades out eastwards in the southern region and, although less clearly, also in the North in localities (Paso de los Indios) farther from the trench.

The simplest interpretation for the eastwards fading of the slab imprint is interference with an asthenospheric alkali basalt component that by reaction, may have rapidly evolved to a silica-rich composition. In the South, a similar decrease of the slab signature in the backarc basalts was interpreted as caused by a slab window induced by the subduction of the Chile ridge (Ramos and Kay, 1992; Gorring et al., 1997). In the North, it could be related with asthenosphere flow between the South America lithosphere and the subducted plate (De Ignacio et al., 2001; Gvitzman and Nur, 1999). The alkali basalt component (consistent also with the TiO_2 enrichment observed in three G. Gregores 1B xenoliths, Figs. 3 and 5) was eventually CO_2-rich, in order to justify the wehrlites previously discussed. In both the northern and southern region, however, the occurrences apparently affected by alkali basalt metasomatism have both high Th,U in pyroxenes and high Cl concentrations in the apatites and in the amphiboles (at G. Gregores). Although LILE (and LREE) enrichment is found also in regions where subduction is not active (e.g. Massif Central, France; Lenoir et al., 2000) and Cl may have various origins (Schiano et al., 1994), they are typical of subducted slab-derived components because of hydrothermal alteration of the ocean floor before subduction. Cl is abundantly documented in fluid inclusions in eclogites related to subduction environments (Philippot and Selverstone, 1991; Scambelluri et al., 1997; Philippot et al., 1998). Therefore, as proposed by Laurora et al. (2001), the LILE-enrichment and the abundance of Cl and H_2O may be the only, weak signature of a slab component. In regions far from the trench, where the wedge is very thick, slab components may have fertilised deep, garnet-facies domains of the wedge astenosphere (Yaxley and Green, 1998; Rapp et al., 1999). Small volume melts, having a slab signature, in equilibrium with the fertilised peridotite at the solidus, are ne-normative, (Yaxley and Green, 1998, experiments at 3.5 GPa), but would become silica-saturated during their upward percolation and reaction with the ambient spinel-facies peridotite, up to the region where they trigger melting. In terms of the proposed model (Fig. 15), this stage is referred to the asthenosphere occurring beneath the region of thermal inversion.

The age of the metasomatic imprint in the mantle wedge is unknown and subduction has been repeatedly active since Mesozoic (Ramos and Aleman, 2000). If mantle metasomatism recorded in the southern region is older than 14 Ma,

the Chile Ridge would have been at 50° lat. S and both the northern and southern regions would have been subducted by the Nazca plate. Because of the angle between the Chile ridge and the trench (Fig. 1) the subducted slab would have been older and colder in the North with respect to the South. This may have resulted in different subduction angles and thermal structures of the wedge, with consequent variation in the size and position of the wedge asthenosphere, more shallow in the southern region.

11. Summary and conclusions

The predominant texture in the xenoliths of the nine localities here examined is the re-crystallised granular or the porphyroblastic one. As far as these localities may represent the whole Patagonia mantle, this suggests that the mantle wedge experienced a regional, pervasive re-crystallisation that left only a few relics of the preceding mantle (in our collection, only six samples with protogranular or porphyroclastic texture; group 2).

Dominant rock types are anhydrous lherzolites and harzburgite, rare dunites (group 1A), paralleling at slightly higher concentration the trends of basaltophyle elements worldwide observed in xenolith occurrences or peridotite massifs. Their bulk-rock and clinopyroxene trace element profiles vary from slightly LREE-depleted to LREE-enriched, being LILE-enriched in both cases.

Another recrystallised xenolith group (lherzolites, harzburgites and rare wehrlites, group 1B) contains hydrous phase (amphibole ± phlogopite ± apatite) and is abundantly represented only at G. Gregores. With respect to the anhydrous group, these xenoliths are enriched in Na_2O and CaO, depleted in TiO_2 and Al_2O_3 and have on average lower Mg# values in clinopyroxene. This group also exhibits in both bulk-rock and clinopyroxene a convex upwards trace element pattern resembling that of peridotites affect by alkali basalt metasomatism, but characterised by variable, and sometimes high Ti, Hf and Zr depletion and Nb enrichment.

In both the 1A and B groups, texture and trace element distribution suggest conditions close to equilibrium between the peridotite-forming minerals. Because of this, the orthopyroxene geochemistry, although not specifically discussed, provides indications similar to those of the coexisting clinopyroxene.

Interpretation of the geochemical trends and modelling suggest that the geochemistry of the 1A xenoliths is controlled by two main processes: (1) melting triggered by the addition of a metasomatic component; (2) reactive porous flow of the partial melts thus formed. Process 1 is documented by the correspondence of the geochemical variation trends of the least incompatible elements (HREE, Y and Ti) of bulk-rock and clinopyroxenes with model melting and by the enrichment of LILE and the other highly incompatible elements with respect to the model melting trends. Process 2 refers to the 1A xenoliths containing LREE-enriched clinopyroxenes and to group 1B. The results of AFC modelling are consistent with metasomatism operated by the melts formed during process 1, percolating into a matle segment below its solidus temperature. The HFSE fractionation observed in the group 1B xenoliths is the consequence of the appearance of amphibole when the stability conditions of this phase are reached during percolation. The problem of the negative Zr and Hf anomalies remains, however, open.

The composition of potential melts in equilibrium with clinopyroxene is similar to the Patagonia arc magmas in the occurrences closer to the trench, but in the region South of latitude 46.30°S, it changes eastwards to E-MORB-like by fading of the Nb depletion. This happens, although less clearly, also in northern Patagonia at higher distance from the trench. It is, therefore, proposed that the component triggering melting is slab-derived in the western occurrences and in the eastern ones, an asthenosphere-derived basalt bearing a weak slab signature in its LILE, Cl and H_2O enrichment.

In terms of wedge stratigraphy, the region where melting occurred may be that of thermal inversion and the region recording reactive porous flow the overlaying mantle segment. The group 2 xenoliths may represent the uppermost, cold lithosphere percolated only by ephemeral, residual melts that by chromatographic trace element fractionation, induced the V-shaped trace element patterns observed in the group 2 clinopyroxenes.

The eastward fading of the slab imprint, observed also in the backarc basalts (Stern et al., 1990; Gorring and Kay, 2001), may be consequent to the eastwards wedge thickening and provenance of the metasomatic agent from garnet-facies asthenosphere fertilised by a slab component. Differences in the regional extent of wedge interaction with silica-rich, slab-derived melts between northern and southern Patagonia are tentatively attributed to the subduction of older and colder segments of the Nazca plate in the North with respect to the South, that influence the subduction angle and size and position of the asthenosphere domain in the wedge.

Acknowledgements

We are grateful to E. Bonatti for his helpful critical reading and substantial improvement of the English language. We thank the FOMICRUZ agency, R. Barrenechea and E. Aragon for the facilities and help they provided during the fieldwork in Patagonia. We much appreciate the constructive reviews by M.L. Gorring and L. Lopez Escobar, and of M. Grégoire, S.M. Kay and D.A. Ionov on an earlier version of the manuscript, which helped to substantially improve the paper. We are grateful to Mrs M. Bertacchini for drawing the map in Fig. 1. The assistance of Mr G. Taylor in the linguistic correction of the manuscript

is gratefully acknowledged. This research was financially supported by MURST (COFIN 1998 and 2000), CNR and CNR-CONICET joint programmes.

References

Baker, M.B., Stolper, E.M., 1994. Determining the composition of high-pressure mantle melts using diamond aggregates. Geochim. Cosmochim. Acta 58, 2811–2827.

Bedini, R.M., Bodinier, J.-L., Dautria, Jm.M., Morten, L., 1997. Evolution of LILE-enriched small melt fractions in the lithospheric mantle: a case study from the East African Rift. Earth Planet. Sci. Lett. 153, 67–83.

Bizimis, M., Salters, V.J.M., Bonatti, E., 2000. Trace and REE content of clinopyroxenes from supra-subduction zone peridotites. Implications for melting and enrichment processes in island arcs. Chem. Geol. 165, 67–85.

Bodinier, J.L., Dupuy, C., Dostal, J., 1988. Geochemistry and petrogenesis of Eastern Pyrenean peridotites. Geochim. Cosmochim. Acta 52, 2893–2907.

Bottazzi, P., Ottolini, L., Vannucci, R., Zanetti, A., 1994. An accurate procedure for the quantification of rare earth elements in silicates. In: Benninghoven, A., Nihei, A.Y., Shimizu, N., Werner, H.W. (Eds.), Secondary Ion Mass Spectrometry, SIMS IX Proceedings. Wiley, New York, pp. 927–930.

Bottazzi, P., Tiepolo, M., Vannucci, R., Zanetti, A., Brumm, R., Foley, S.F., Oberti, R., 1999. Distinct site preferences for heavy and light REE in amphibole and the prediction of $^{Amph/L}D_{REE}$. Contrib. Mineral. Petrol. 137, 36–45.

Brey, G.P., Köhler, T.P., 1990. Geothermobarometry in four-phase lherzolites II. New thermobarometers and practical assessment of existing thermobarometers. J. Petrol. 31, 1353–1378.

Cande, S.C., Leslie, R.B., 1986. Late Cenozoic tectonics of the southern Chile Trench. J. Geophys. Res. 91, 495–520.

Carroll, M.R., Wyllie, P.J., 1989. Experimental phase relations in the system Tonalite-Peridotite-H_2O at 15 kb; implications for assimilation and differentiation processes near the crust-mantle boundary. J. Petrol. 30, 1351–1382.

Chalot-Prat, F., Boullier, A.-M., 1997. Metasomatism in the sub-continental mantle beneath the Eastern Carpathians (Romania): new evidence from trace element geochemistry. Contrib. Mineral. Petrol. 129, 284–307.

Churikova, T., Dorendorf, F., Worner, G., 2001. Sources and fluids in the mantle wedge below Kamchatka, evidence from across-arc geochemical variation. J. Petrol. 42, 1567–1593.

Ciuffi, S., Rivalenti, G., Vannucci, R., Zanetti, A., Mazzucchelli, M., Cingolani, C.A., 2002a. Geochemical Variations in the Host Basalt-Derived Glasses Infiltrating Mantle Xenoliths. Actas del XV Congreso Geologico Argentino, El Calafate 2002, Tomo III, pp. 83–84.

Ciuffi, S., Rivalenti, G., Vannucci, R., Zanetti, A., Mazzucchelli, M., Cingolani, C.A., 2002b. Are the glasses in mantle xenoliths witness of the metasomatic agent composition? Godschmidt Conference, Davos, Switzerland. Conference Abstracts, Special Supplement. Geochim. Cosmochim. Acta 66, A143.

Comin-Chiaramonti, P., Princivalle, F., Girardi, V.A.V., Gomes, C.B., Laurora, A., Zanetti, A., 2001. Mantle xenoliths from Nemby. Eastern Paraguay: O–Sr–Nd isotopes, trace elements and crystal chemistry of hosted clinopyroxenes. Per. Mineral. 70, 205–230.

Davies, J.H., Stevenson, D.J., 1992. Physical model of source region of subduction zone volcanics. J. Geophys. Res. 97, 2037–2070.

De Ignacio, C., Lopez, I., Oyarzum, R., Marquez, A., 2001. The northern Patagonia Somuncura plateau basalts: a product of slab-induced, shallow asthenospheric upwelling? Terra Nova 13, 117–121.

DePaolo, D.J., 1981. Trace element and isotopic effects of combined wallrock assimilation and fractional crystallization. Earth Planet. Sci. Lett. 53, 189–202.

D'Orazio, M., Agostini, S., Mazzarini, F., Innocenti, F., Manetti, P., Haller, M.J., Lahsen, A., 2000. The Pali Aike volcanic field, Patagonia: slab-window magmatism near the tip of South America. Tectonophysics 321, 407–427.

D'Orazio, M., Agostini, S., Innocenti, F., Haller, M.J., Manetti, P., Mazzarini, F., 2001. Slab window-related magmatism from southermost South america: the late Miocene volcanics from the Estancia Glencross area s(52°S, Argentina–Chile). Lithos 57, 67–89.

Ewart, A., Collerson, K.D., Regelous, M., Wendt, J.I., Niu, Y., 1998. Geochemical evolution within the Tonga-Kermadec-Lau arc-back-arc systems: the role of varying mantle wedge composition in space and time. J. Petrol. 39, 331–368.

Fabriès, J., Bodinier, J.L., Dupuy, C., Lorand, J.P., Benkerrou, C., 1989. Evidence for modal metasomatism in the orogenic spinel lherzolite body from Caussou (Northeastern Pyrenees, France). J. Petrol. 30, 176–199.

Foley, S.F., Petibon, C.M., Jenner, G.A., Kjarsgaard, B.A., 2001. High U/Th partitioning by clinopyroxene from alkali silicate and carbonatite metasomatism: an origin for Th/U disequilibrium in mantle melts? Terra Nova 13, 104–109.

Forsythe, R.D., Nelson, E.P., Carr, M.J., Kaeding, M.E., Hervé, M., Mpodozis, C., Soffia, J.M., Harambour, S., 1986. Pliocene near-trench magmatism in southern Chile: a possible manifestation of ridge collision. Geology 14, 23–27.

Franzini, M., Leoni, L., Saitta, M., 1975. Revisione di una metodologia analitica per fluorescenza-X, basata sulla correzione completa degli effetti di matrice. Rend. Soc. Ital. Mineral. Petrol. 31, 365–379.

Gaetani, G.A., Grove, T.L., 1998. The influence of water on melting of mantle peridotite. Contrib. Mineral. Petrol. 131, 323–346.

Gorring, M.L., Kay, S.M., 2000. Carbonatite metasomatized peridotite xenoliths from southern Patagonia: implications for lithospheric processes and Neogene plateau magmatism. Contrib. Mineral. Petrol. 140, 55–72.

Gorring, M.L., Kay, S.M., 2001. Mantle processes and sources of Neogene slab window magmas from southern Patagonia. Argent. J. Petrol. 42, 1067–1094.

Gorring, M.L., Kay, S.M., Zitler, P.K., Ramos, V.A., Rubiolo, D., Fernandez, M.I., Panza, J.L., 1997. Neogene Patagonian plateau lavas: continental magmas associated with ridge collision at the Chile triple junction. Tectonics 16, 1–17.

Green, D.H., 1973. Experimental melting studies on a model upper mantle composition at high pressure under water-saturated and water-undersaturated conditions. Earth Planet. Sci. Lett. 19, 37–53.

Green, T.H., Blundy, J.D., Adam, J., Yaxley, G.M., 2000. SIMS determination of trace element partition coefficients between garnet, clinopyroxene and hydrous basaltic liquids at 2–7.5 GPa and 1080–1200 °C. Lithos 53, 165–187.

Grégoire, M., Moine, B.N., O'Reilly, S.Y., Cottin, J.Y., Giret, A., 2000. Trace element residence and partitioning in mantle xenoliths metasomatized by highly alkaline, silicate- and carbonate-rich melts (Kerguelen Islands, Indian Ocean). J. Petrol. 41, 477–509.

Grégoire, M., McInnes, B.I.A., O'Reilly, S.Y., 2001. Hydrous metasomatism of oceanic sub-arc mantle. Lihir, Papua, New Guinea. Part 2. Trace element characteristics of slab-derived fluids. Lithos 59, 91–108.

Gvitzman, Z., Nur, A., 1999. Plate detachment, asthenosphere upwelling, and topography across subduction zones. Geology 27, 563–566.

Hart, S.R., Dunn, T., 1993. Experimental cpx/melt partitioning of 24 trace elements. Contrib. Mineral. Petrol. 113, 1–8.

Hauri, E.H., Shimizu, N., Dieu, J.J., Hart, S.R., 1993. Evidence for hot-spot-related carbonatite metasomatism in the oceanic upper mantle. Nature 365, 221–227.

Hellebrand, E., Snow, J.E., Dick, H.J.B., Hofmann, A.W., 2001. Coupled major and trace elements as indicators of the extent of melting in mid-ocean-ridge peridotites. Nature 410, 677–681.

Hellebrand, E., Snow, J.E., Műhe, R., 2002. Mantle melting beneath Gakkel Ridge (Arctic Ocean): abyssal peridotite spinel compositions. Chem. Geol. 182, 227–235.

Hickey, R.L., Frey, F.A., Gerlach, D.C., López-Escobar, L., 1986. Multiple sources for basaltic arc rocks from the southern volcanic zone of the Andes (34°–41°S): trace element and isotopic evidence for contributions from subducted oceanic crust, mantle, and continental crust. J. Geophys. Res. 91, 5963–5983.

Hirose, K., Kawamoto, T., 1995. Hydrous partial melting of lherzolite at 1 GPa: the effect of H_2O on the genesis of basaltic magmas. Earth Planet. Sci. Lett. 133, 463–473.

Hirschmann, M.M., Baker, M.B., Stolper, E.M., 1998. The effect of alkalis on the silica content of mantle-derived melts. Geochim. Cosmochim. Acta 62, 883–902.

Hofmann, A.W., 1988. Chemical differentiation of the Earth: the relationship between mantle, continental crust and oceanic crust. Earth Planet. Sci. Lett. 90, 297–314.

Ionov, D.A., Bodinier, J.L., Mukasa, S.B., Zanetti, A., 2002. Mechanisms and sources of mantle metasomatism: major and trace element compositions of peridotite xenoliths from Spitsbergen in the context of numerical modelling. J. Petrol. 43, 1–41.

Irvine, T.N., 1975. Crystallization sequences in the Muskox intrusion and other layered intrusions-II. Origin of chromitite layers and similar deposits of other magmatic ores. Geochim. Cosmochim. Acta 39, 991–1020.

Irvine, T.N., 1977. Origin of chromitite layers in the Muskox intrusion and other stratiform intrusions: a new interpretation. Geology 5, 273–277.

Jenner, G.A., Longerich, H.P., Jackson, S.E., Fryer, B.J., 1990. ICP-MS—A powerful tool for high-precision trace-element analysis in earth sciences: evidence from analysis of selected U.S.G.S. reference samples. Chem. Geol. 83, 133–148.

Johnson, K.T.M., Dick, H.J.B., 1992. Open system and temporal and spatial variation of peridotite and basalt of the Atlantis II fracture zone. J. Geophys. Res. 97, 9219–9241.

Johnson, K.T.M., Dick, H.J.B., Shimizu, N., 1990. Melting in oceanic upper mantle: an ion microprobe study of diopsides in Abyssal Peridotites. J. Geophys. Res. 95, 2661–2678.

Kay, S.M., 2002. Magmatic Sources. Tectonic Setting and Causes of Tertiary to Recent Patagonian Plateau Magmatism (36°S to 52°S latidude). Actas del XV Congreso Geologico Argentino, El Calafate 2002, Tomo III, pp. 95–100.

Kay, S.M., Ardolino, A.A., Franchi, M., Ramos, V.A., 1993a. El origen de la meseta de Sumun Cura: distribucion de sus rocas volcanicas maficas. XII Congreso Geologico Argentino y II Congreso de hydrocarburos. Actas I° (IV), 236–248.

Kay, S.M., Ramos, V.A., Marquez, M., 1993b. Evidence in Cerro Pampa volcanic rocks for slab-melting prior to ridge-trench collision in southern South America. J. Geol. 101, 703–714.

Kelemen, P.B., 1995. Genesis of high Mg# andesites and the continental crust. Contrib. Mineral. Petrol. 120, 1–19.

Kelemen, P.B., Whitehead, J.A., Aharonov, E., Jordahl, K.A., 1995. Experiments on flow focusing in soluble porous media, with applications to melt extraction from the mantle. J. Geophys. Res. 100, 475–496.

Kelemen, P.B., Hart, S.R., Bernstein, S., 1998. Silica enrichment in the continental upper mantle via melt/rock reaction. Earth Planet. Sci. Lett. 164, 387–406.

Kempton, P.D., Hawkesworth, C.J., Lopez-Escobar, L., Pearson, D.G., Ware, A.J., 1999. Spinel ± garnet lherzolite xenoliths from Pali aike: part 2. Trace element and isotopic evidence bearing on the evolution of lithospheric mantle beneath southern Patagonia. In: Gurney, J.J., Gurney, J.L., Pascoe, M.D., Richardson, S.H. (Eds.), The J.B. Dawson Volume. Proceedings of International Kimberlite Conference 7. vol. 1., pp. 415–428.

Kepezhinskas, P., Defant, M.J., Drummomd, M.S., 1995. Na metasomatism in the island-arc mantle by slab melt-peridotite interaction: evidence from mantle xenoliths in the north Kamchatka Arc. J. Petrol. 36, 1505–1527.

Kepezhinskas, P., Defant, M.J., Drummomd, M.S., 1996. Progressive enrichment of island arc mantle by melt-peridotite interaction inferred from Kamchatka xenoliths. Geochim. Cosmochim. Acta 60, 1217–1229.

Kilian, R., Weigand, O., Altherr, R., 1997. Tertiary to Quaternary Chemical Trends of Basalts from the Cordillera Baguales (50°S): Constraints on the Geotectonic Evolution of the Southernmost Andes. Final Symposium IGCP 345 Evoluciòn Litosférica de los Andes. Actas VIII Congreso Geologico Chileno 3, pp. 1666–1670.

Kilian, R., Franzen, C., Koch, M., 1998. The metasomatism of the mantle wedge below the southern Andes: constraints from laser ablation microprobe ICP-MS trace element analysis of clinopyroxenes, orthopyroxenes and fluid inclusions of mantle xenoliths. Terra Nostra 98/5, 81–82.

Kinzler, R.J., 1997. Melting of mantle peridotite at pressures approaching the spinel to garnet transition: application to mid-ocean ridge basalt petrogenesis. J. Geophys. Res. 102, 853–874.

Köhler, T.P., Brey, G.P., 1990. Calcium exchange between olivine and clinopyroxene calibrated as a geothermobarometer for natural peridotites from 2 to 60 kb with applications. Geochim. Cosmochim. Acta 54, 2375–2388.

Kretz, R., 1983. Symbols of rock-forming minerals. Am. Mineral. 68, 277–279.

Kushiro, I., 1969. The system forsterite-diopside-silica with and without water at high pressures. Am. J. Sci. 267, 269–294.

Laurora, A., Mazzucchelli, M., Rivalenti, G., Vannucci, R., Zanetti, A., Cingolani, C.A., 2000. Melt migration in the mantle wedge: a case study from Patagonia back-arc. Godschmidt 2000. J. Conference Abstr. 5(2), 624.

Laurora, A., Mazzucchelli, M., Rivalenti, G., Vannucci, R., Zanetti, A., Barbieri, M.A., Cingolani, C.A., 2001. Metasomatism and melting in carbonated peridotite xenoliths from the mantle wedge: the Gobernador Gregores case (Southern Patagonia). J. Petrol. 42, 69–87.

LeMaitre, R.W., 1979. A new generalised petrological mixing model. Contrib. Mineral. Petrol. 71, 133–137.

Lenoir, X., Garrido, C.J., Bodinier, J.-L., Dautria, J.-M., 2000. Contrasting lithospheric mantle domains beneath the Massif Central (France) revealed by geochemistry of peridotite xenoliths. Earth Planet. Sci. Lett. 181, 359–375.

Leoni, L., Saitta, M., 1976. X-ray fluorescence analysis of 29 trace elements in rock and mineral standards. Rend. Soc. Ital. Mineral. Petrol. 32, 497–510.

Mercier, J.-C.C., 1980. Single-pyroxene thermobarometry. Tectonophysics 70, 1–37.

Moine, B.N., Grégoire, M., O'Reilly, S.Y., Sheppard, S.M.F., Cottin, J.Y., 2001. High field strength element fractionation in the upper mantle: evidence from amphibole-rich composite mantle xenoliths from the Kerguelen Islands (Indian Ocean). J. Petrol. 42, 2145–2167.

Navon, O., Stolper, E., 1987. Geochemical consequences of melt percolation: the upper mantle as a chromatographic column. J. Geol. 95, 285–307.

Niu, Y., 1997. Mantle melting and melt extraction processes beneath ocean ridges: evidence from abyssal peridotites. J. Petrol. 38, 1047–1074.

Norman, M.D., 1998. Melting and metasomatism in the continental lithosphere: laser ablation ICPMS analysis of minerals in spinel lherzolites from eastern Australia. Contrib. Mineral. Petrol. 130, 240–255.

Parkinson, I.J., Pearce, J.A., 1998. Peridotites from the Izu-Bonin-Mariana forearc (ODP Leg 125): evidence for mantle melting and melt-mantle interaction in a supra-subduction zone setting. J. Petrol. 39, 1577–1618.

Philippot, P., Selverstone, J., 1991. Trace-element-rich brines in eclogitic veins: implications for fluid composition and transport during subduction. Contrib. Mineral. Petrol. 106, 417–430.

Philippot, P., Agrinier, P., Scambelluri, M., 1998. Chlorine cycling during subduction of altered oceanic crust. Earth Planet. Sci. Lett. 161, 33–44.

Popp, R.K., Frantz, J.D., 1990. Fluid Immiscibility in the System H_2O–Nacl–CO_2 as Determined from Synthetic Fluid Inclusions. Carnegie Institution of Washington, Annual report 1989–1990, pp. 43–48.

Raffone, N., Zanetti, A., Chazot, G., Pin, C., Vannucci, R., 2002. The Composition and Evolution of the Lithospheric Mantle Beneath Mid

Atlas (Morocco). Fourth International Workshop on Orogenic Lherzolites and Mantle Processes, Abstract Volume, pp. 127.

Ramos, V.A., Aleman, A., 2000. Tectonic Evolution of the Andes. In: Cordani, U.G., Milani, E.J., Thomas Filho, A., Campos, D.A. (Eds.), Tectonic Evolution of South America. International Geological Congress, Rio de Janeiro, pp. 635–685.

Ramos, V.A., Kay, S.M., 1992. Southern Patagonia plateau basalts and deformation: backarc testimony of ridge collisions. Tectonophysics 205, 261–282.

Rampone, E., Bottazzi, P., Ottolini, L., 1991. Complementary Ti and Zr anomalies in orthopyroxene and clinopyroxene from mantle peridotites. Nature 354, 518–521.

Rapp, R.P., Shimizu, N., Norman, M.D., Applegate, G.S., 1999. Reaction between slab-derived melts and peridotite in the mantle wedge: experimental constraints at 3.8 GPa. Chem. Geol. 160, 335–356.

Rivalenti, G., Mazzucchelli, M., 2000. Interaction of mantle-derived magmas and crust in the Ivrea-Verbano zone and the Ivrea mantle peridotites. In: Ranalli, G., Ricci, C.A., Trommsdorff, V. (Eds.), Crust-Mantle Interactions. Proceedings of International School Earth Planet Sci., Siena, pp. 153–198.

Rivalenti, G., Mazzucchelli, M., Girardi, V.A.V., Vannucci, R., Barbieri, M.A., Zanetti, A., Goldstein, S.L., 2000. Composition and processes of the mantle lithosphere in northeastern Brazil and Fernando de Noronha: evidence from mantle xenoliths. Contrib. Mineral. Petrol. 138, 308–325.

Rudnick, R.L., McDonough, W.F., Chappell, B.C., 1993. Carbonatite metasomatism in the northern Tanzanian mantle. Earth Planet Sci. Lett. 114, 463–475.

Scambelluri, M., Piccardo, G.B., Philippot, P., Robbiano, A., Negretti, L., 1997. High salinity fluid inclusions formed from recycled seawater in deeply subducted alpine serpentinite. Earth Planet Sci. Lett. 148, 485–499.

Schiano, P., Clocchiatti, R., Shimizu, N., Weis, D., Mattielli, N., 1994. Cogenetic silica-rich and carbonate-rich melts trapped in mantle minerals in Kerguelen ultramafic xenoliths: implications for metasomatism in the oceanic upper mantle. Earth Planet Sci. Lett. 123, 167–178.

Shaw, D.M., 1970. Trace element fractionation during anatexis. Geochim. Cosmochim. Acta 34, 237–243.

Stern, C.R., Kilian, R., 1996. Role of the subducted slab, mantle wedge and continental crust in the generation of adakites from the Andean Austral volcanic zone. Contrib. Mineral. Petrol. 123, 263–281.

Stern, C.R., Saul, S., Skewes, M.A., Futa, K., 1989. Garnet peridotite xenoliths from the Pali Aike basalts of southernmost South America. In: 'Kimberlites and Related Rocks'. Geol. Soc. Australia, pec. Publ. 14. Blackwell, Carlton, Australia 2, pp. 735–744.

Stern, C.R., Frey, F.A., Futa, K., Zartman, R.E., Peng, Z., Kyser, T.K., 1990. Trace-element and Sr, Nd, Pb, and O isotopic composition of Pliocene and Quaternary alkali basalts of the Patagonia Plateau lavas of southernmost South America. Contrib. Mineral. Petrol. 104, 294–308.

Stern, C.R., Kilian, R., Olker, B., Hauri, E.H., Kyser, T.K., 1999. Evidence from mantle xenoliths for relatively thin (<100 km) continental lithosphere below the phanerozoic crust of southernmost South America. Lithos 48, 217–235.

Sun, S.-s., McDonough, W.F., 1989. Chemical and isotopic systematics of ocean basalts: implications for mantle composition and processes. In: Saunders, A.D., Norry, M.J. (Eds.), Magmatism in the Ocean Basins. Geol. Soc. Spec. Publ., 42, pp. 313–345.

Takazawa, E., Frey, F.A., Shimizu, N., Obata, M., 2000. Whole rock compositional variations in an upper mantle peridotite (Horoman, Hokkaido, Japan: are they consistent with a partial melting process? Geochim. Cosmochim. Acta 64, 695–716.

Tiepolo, M., Vannucci, R., Oberti, R., Foley, S., Bottazzi, P., Zanetti, A., 2000. Nb and Ta incorporation and fractionation in Ti-rich pargasite and kaersutite: crystal-chemical constraints and implications for natural systems. Earth Planet Sci. Lett. 176, 185–201.

Tiepolo, M., Bottazzi, P., Foley, S., Oberti, R., Vannucci, R., Zanetti, A., 2001. Fractionation of Nb and Ta from Zr and Hf at mantle depths: the role of titanian pargasite and kaersutite. J. Petrol. 42, 221–232.

Vannucci, R., Bottazzi, P., Wulff-Pedersen, E., Neumann, E-R., 1998. Partitioning of REE, Y, Sr, Zr and Ti between clinopyroxene and silicate melts in the mantle under La Palma (Canary Islands): implications for the nature of the metasomatic agents. Earth Planet Sci. Lett. 158, 39–51.

Vernières, J., Godard, M., Bodinier, J.-L., 1997. A plate model for the simulation of trace element fractionation during partial melting and magma transport in the earth's upper mantle. J. Geophys. Res. 102, 24771–24784.

Witt-Eickshen, G., Harte, B., 1994. Distribution of trace elements between amphibole and clinopyroxene from mantle peridotites of the Eifel (Western Germany). Chem. Geol. 117, 235–250.

Xu, Y.-G., Menzies, M.A., Bodinier, J.-L., Bedini, R.M., Vroon, P., Mercier, J.-C.C., 1998. Melt percolation and reaction atop a plume: evidence from the poikiloblastic peridotite xenoliths from Borée (Massif Central,. France). Contrib. Mineral. Petrol. 132, 65–84.

Xu, X., O'Reilly, S.Y., Griffin, W.L., Zhou, X., 2000. Genesis of young lithospheric mantle in southeastern China: an LAM-ICPMS trace element study. J. Petrol. 41, 111–148.

Yaxley, G.M., Green, D.H., 1998. Reactions between eclogite and peridotite: mantle refertilisation by subduction of oceanic crust. Schweiz. Mineral. Petrogr. Mitteil. 78, 243–255.

Yaxley, G.M., Crawford, A.J., Green, D.H., 1991. Evidence for carbonatite metasomatism in spinel peridotite xenoliths from Western Victoria, Australia. Earth Planet Sci. Lett. 107, 305–317.

Zanetti, A., Mazzucchelli, M., Rivalenti, G., Vannucci, R., 1999. The finero phlogopite-peridotite massif: an example of subduction-related metasomatism. Contrib. Mineral. Petrol. 134, 107–122.